

CHARACTERIZATION OF GLASS MICROSPHERES FOR CANCER
HYPERTHERMIA

BY

JEFFREY DANEAULT

A THESIS
SUBMITTED TO THE FACULTY OF

ALFRED UNIVERSITY

IN PARTIAL FULFILLMENT OF THE REQUIREMENTS
FOR THE DEGREE OF

MASTER OF SCIENCE

IN

MATERIALS SCIENCE AND ENGINEERING

ALFRED, NEW YORK

MAY, 2019

CHARACTERIZATION OF GLASS MICROSPHERES FOR CANCER
HYPERThERMIA

BY

JEFFREY DANEAULT

B.S. ALFRED UNIVERSITY [2017]

SIGNATURE OF AUTHOR _____

APPROVED BY _____

DR. ANTHONY WREN, ADVISOR

DR. TIMOTHY KEENAN, ADVISORY COMMITTEE

DR. WILLIAM LACOURSE, ADVISORY COMMITTEE

DR. HOLLY SHULMAN, CHAIR, ORAL THESIS DEFENSE

ACCEPTED BY _____

GABRIELLE GAUSTAD, DEAN
KAZUO INAMORI SCHOOL OF ENGINEERING

Alfred University theses are copyright protected and may be used for education or personal research only. Reproduction or distribution in part or whole is prohibited without written permission from the author.

Signature page may be viewed at Scholes Library, New York State College of Ceramics, Alfred University, Alfred, New York.

ACKNOWLEDGMENTS

There are many people that I would like to thank for supporting me along my journey towards my degree. First I would like to thank my advisor Dr. Anthony Wren who for the past 3 years has been a mentor for me in the biomaterial sciences and who has helped shape the way I think as a materials scientist. I would also like to thank the members of my committee, Dr. Timothy Keenan and Dr. William LaCourse. Dr. Keenan has been a wonderful help in training my lab skills and allowing me to take ownership over some of the complicated pieces of machinery in the lab. Dr. LaCourse has inspired my creative side of science and has always given me a wealth of knowledge for the glass sciences. Many other faculty staff at Alfred have been instrumental in me reaching this milestone of my life. Dr. Darren Stohr building my SEM skills, Dr. Steven Tidrow enabling me to increase the safety of my research, Emilie Carney and Laura Grove for helping me navigate my way towards this degree, and countless others whose short interactions have had great impact. I would also like to thank all my fellow students who have shaped my growth. Having friendly faces in and out of the labs has always been a great motivator for me and is deeply appreciated. I additionally would like to thank my friends from home, especially Brian Lee and my brother Greg. Having an outlet away from the work is an important part of my life and I am glad we remained close, even from 300 miles away. Last and certainly not least I would like to thank my mom Fran and dad Steve. They have always been supportive of me and my endeavors and have really helped me push myself academically.

TABLE OF CONTENTS

	Page
<i>Acknowledgments</i>	<i>iii</i>
<i>Table of Contents</i>	<i>iv</i>
<i>List of Tables</i>	<i>vi</i>
<i>List of Figures</i>	<i>vii</i>
ABSTRACT	X
I. INTRODUCTION	1
A. BIOMATERIALS FROM GLASS	1
B. HYPERTHERMAL CANCER TREATMENT	2
C. HISTORY OF HYPERTHERMIA TREATMENT	5
D. MAGNETIC HYPERTHERMIA.....	7
E. MAGNETIC RESONANCE IMAGING	9
F. GADOLINIUM	10
G. HOLMIUM	12
H. IRON AND MANGANESE.....	12
I. OBJECTIVE	13
II. EXPERIMENTAL PROCEDURE	14
A. MATERIAL SYNTHESIS	14
1. <i>Glass Powder Synthesis</i>	14
2. <i>Glass Microsphere Synthesis</i>	Error! Bookmark not defined.
B. GLASS POWDER CHARACTERIZATION.....	16
1. <i>X-Ray Diffraction (XRD)</i>	16
2. <i>Thermal Analysis</i>	17
3. <i>X-Ray Photoelectron Spectroscopy (XPS)</i>	17
4. <i>Advanced Surface Area and Porosity (ASAP)</i>	17
5. <i>Glass Particle Solubility and Ion Release</i>	17
C. GLASS MICROSPHERE CHARACTERIZATION	18
1. <i>Optical Microscopy</i>	18
2. <i>Corrosion Study</i>	18
3. <i>Scanning Electron Microscopy (SEM) and Energy Dispersive X-Ray Analysis (EDX)</i>	18

III. RESULTS AND DISCUSSION	19
A. GLASS POWDER CHARACTERIZATION.....	19
1. <i>X-Ray Diffraction (XRD)</i>	19
2. <i>Thermal Analysis</i>	22
3. <i>X-Ray Photoelectron Spectroscopy (XPS)</i>	24
B. GLASS CORROSION STUDIES	30
1. <i>Glass Particle Solubility and Ion Release</i>	30
C. GLASS MICROSPHERE CHARACTERIZATION	33
1. <i>Optical Microscopy</i>	33
2. <i>Corrosion Study</i>	37
3. <i>Scanning Electron Microscopy (SEM) and Energy Dispersive X-Ray Analysis (EDX)</i>	40
IV. SUMMARY AND CONCLUSIONS.....	47
V. FUTURE WORK	49
VI. REFERENCES	51

LIST OF TABLES

	Page
Table I Naming Convention. Glass nomenclature and Composition of the Glasses	16
Table II Glass Transition Temperatures of Glass Powders	24
Table III Bonding and Non-Bonding Oxygen levels for Glass Powder Samples.....	29

LIST OF FIGURES

	Page
Figure 1. Effect of temperature and time on the survival of different cell lines. ¹³	4
Figure 2. Typical hysteresis loop. ³⁵	8
Figure 3. Neel relaxation (above) and Brownian relaxation (below) with the arrow depicting superspin direction.	9
Figure 4. MRI of heart tissue, before and after P792 contrast agent administration. ⁴²	11
Figure 5. X-Ray Diffraction patterns of glass powder samples. Top: Gd and bottom: Ho.....	20
Figure 6. X-Ray Diffraction patterns of glass powder samples. Top Fe and bottom: Mn.....	21
Figure 7. Heat flow curves from glass powders.	22
Figure 8. Glass transition temperatures of glass powders.....	23
Figure 9. Survey XPS scans for Gd glass powders.....	25
Figure 10. Survey XPS scans for Ho glass powders.....	26
Figure 11. Survey XPS scans for Fe glass powders.....	26
Figure 12. Survey XPS scans for Mn glass powders.....	27
Figure 13. High resolution XPS for Gd glass powder. A: 5%, B: 10%, C:15%, and D: 20%.	28
Figure 14. NBO content as a function of substituent concentration.	30
Figure 15 Ion release of Gd powder samples at 1, 10, 100, and 1000 hr: A: Gd, B:Si, and C: Ge, and Ion release of all glass powder samples at 1000 hr: A: Substituent, B:Si, and C: Ge	32

Figure 16. Particle diameter of glass microspheres based on the composition.	33
Figure 17. Reflectance microscopy images of all compositions of microspheres.	34
Figure 18. Diameter of glass microspheres based on the glass transition temperature. ...	35
Figure 19. Optical transmission microscopy of 15 Gd microspheres.	36
Figure 20. Optical transmission microscopy of 15 Ho microspheres.	36
Figure 21. SEM image of 5 Ho spheres after 100 hours in a pH 4 solution. Left and right SE.....	38
Figure 22. SEM image of 15 Ho spheres after 100 hours in a pH 4 solution. Left BSE and right SE.....	38
Figure 23 Lattice corrosion of 15 Gd glass microsphere after 1000 hr in pH 4 solution.....	39
Figure 24 Surface roughness after 1000 hr in solution: left 5 Ho pH 10, right 5 Gd pH 4.....	40
Figure 25. Gd microspheres after production.	41
Figure 26. Atomic concentration of substitute in glass microspheres.	41
Figure 27. Elemental maps of random Gd and Ho microspheres before and after 1000 hours in DI water.	42
Figure 28. Combination BSE and SE of a broad section of microspheres with typical defects listed. Square: un-melted, triangle: shape, star: pores, diamond: air bubbles.....	44
Figure 29. Combination BSE and SE image of a scaffold defect found in 15 Ho (left) and 15 Gd (right) microspheres.	45
Figure 30 Combination BSE and SE image of pocket defect found in 20 Mn (left) and 15 Gd (right).....	46
Figure 31. SEM imaging with secondary electrons of a concave sphere defect.....	46

ABSTRACT

Hyperthermal treatment of cancer has historically been used as an adjuvant to radiotherapy, and while effective it typically was used on near-surface cancers. Synthesis and characterization of glass microspheres to be inserted directly to a cancerous growth was conducted where sixteen compositions of glass were synthesized using the melt-quench method. The compositions were based 30SiO₂-10P₂O₅-25GeO₂-35CaO (mol%) with an increasing 5-20 mol% substituent (Gd₂O₃, Ho₂O₃, Fe₂O₃, and Mn₂O₃) in place of CaO. XRD was conducted on each glass and the samples were found to be semi-crystalline with calcium phosphate peaks. Thermal analysis showed a decrease in T_g with increasing substitution content and the T_g ranged from 590 to 890°C. Ion release studies of 1, 10, 100, and 1000 hr were conducted on the glass powders, and the amount of silica (Si) Ge, and substituent ions were determined. There was a decreasing trend of ion release with increasing gadolinium (Gd) and holmium (Ho) concentrations. The levels of ion release in the iron (Fe) and manganese (Mn) samples may limit their applicability with respect to implantation into the body. The Gd and Ho samples had extremely low ion release rates, even after 1000 hrs incubation in aqueous media. Optical transmission microscopy showed that the glass was successfully converted from particle form into micron sized spheres. The size of the spheres was independent of the T_g or the composition and the overall average diameter of the 16 compositions was 95.6 μm. A corrosion study with pH 4, 7, and 10 solutions, presented very minor traces of degradation on the samples surface post incubation in each pH solution. SEM analysis showed the typical types of defects in the spheres. These defects were total failure to melt, partial melting, surface pores, and air bubbles. There were also atypical scaffold, pocket, and concave defects. Characterization of the glass and microspheres show that there is potential for all the Gd and Ho samples to be used in the body for cancer hyperthermia.

I. INTRODUCTION

A. Biomaterials from Glass

Any type of material that interacts with a biological system is considered to be a biomaterial. Biomaterials can be grouped into three main classes: Bioinert, biocompatible, and bioresorbable. Bioinert materials can be seen in devices like pacemakers, dental crowns, and load bearing implants, just to name a few. The main feature of bioinert materials is that they do not interact chemically with the body.¹ The lack of interaction is a plus in pacemakers and dental materials as these devices need to perform their function for extended periods of time and cannot be worn down by the body. The downside that arises from the inertness is that the body can form a fibrous capsule around the implant. The encapsulation essentially makes the implant be treated as an outside portion of the body. In load bearing implants, being inert is useful as they need to last, but the fibrous capsule segments and reduces the stability possibly causing failure. Often these implants are textured and coated with a biocompatible material to create a strong body material adhesion.² Biocompatible materials are materials that elicit no negative response from the body. There must be no systemic response to the implantation of the material, except for the initial swelling and inflammation associated with the materials implantation.

The most typical glass biomaterial is bioglass, which interacts positively with the body to stimulate bone growth. Bioglass was discovered by Larry Hench in 1969.³ Any material that interacts positively with the body is considered to be bioactive. Bioglass is bioactive as well biodegradable. Even though bioglass stays in the body for years, it slowly degrades to aide in the healing process. Bioglass scaffolds are able to restore 32% of an effected area after six weeks.⁴ Scaffolds are semi-structural materials that can be inserted into bone voids to help improve tissue integration. Scaffolds are porous which allows for easier vascularization. The scaffold structure also helps facilitate the dissolution of the glass network and the migration of calcium (Ca) and phosphorous (P) to the surface.⁵ Bone is primarily composed of Ca and P and so these elements help the bone remodeling cells, osteoblasts and osteoclasts, heal the bone.⁶ Bioglass for bone

repair is not the only use of bioactive materials, dental reconstruction, bone screws, middle ear replacements, and filling agents for vacated tissue are all common uses.⁷

Another application of glass biomaterials are ⁹⁰Y microspheres which have been used for radiotherapy. ⁹⁰Y is an isotope of yttrium that is available as TheraSpheres or as SIR-Spheres.⁸ This isotope is radioactive so it can be used to deliver a concentrated dose of radiation to targeted cancer cells causing death. Radiation, like in chemotherapy, destroys cancerous and healthy cells so delivering the dose directly to the affected area increases efficacy of the treatment.⁹ ⁹⁰Y spheres are used for liver cancer and their short half-life of 64 hours makes them a safe choice.⁹⁻¹¹ Radiotherapy works because the x-rays damage the DNA of cells, stopping all protein function and causing death.¹² These ⁹⁰Y glass spheres are different than bioactive glass, because they do not get resorbed by the body. Glass biomaterials have a vast range of application because of their tunability of ion release.

B. Hyperthermal Cancer Treatment

When it comes to temperature, tumor cells are just like healthy cells. Adding heat will kill the cell by denaturing the proteins inside it. The temperature change increases the amount of thermal energy in the amino acid chain. Increased thermal energy increases the Brownian motion, or the random movements, of the amino acids. This can cause the ionic bonds to be broken, and in some cases reform into different bonds. As the shape of the amino acid chain dictates the shape of the protein, this heat will change the structure of the proteins in the cell and inhibit their functions. Proteins in cells act as ion channels, enzymes, and structural components of the cell. Heat treatments are effective because they can; denature, fold, and aggregate proteins, initiate apoptosis, and cause necrosis.^{13,14} Increasing the temperature is a natural process that the body undergoes when trying to fight against illness. Pyrexia, or fever, is controlled by the hypothalamus and is generally caused by exposure to bacterial byproducts or toxins.¹⁵ Inspired from the body itself, medical therapies have been designed using temperature as the curing agent.

Hyperthermia treatment is the name given to therapies that use an increase in temperature to kill cells. Increasing the body's temperature locally by 5-8°C (9-14.4°F) is the goal in hyperthermal treatment.¹⁶ This increases the cells temperature from 37°C

(98.6°F) to 42-45°C (107.6-113°F). The intensity and duration of the temperature change determines the efficacy of the treatment. Figure 1 presents the effect of heating time on the survivability of adenocarcinoma cells. As seen in Figure 1 it takes significantly less time to kill cancerous cells as the localized temperature is increased, 41-46°C.¹³ At 43°C another factor controlling efficacy is observed, and cell death is effected by the line of cells. While both are colon cells, the WiDr line is less susceptible to heat than the SW 620 line. This difference will be essential to keep in mind when utilizing hyperthermia treatment as the treatment duration will need to be changed based on the cell type to ensure killing enough of the cancerous cells. Above 44°C the degree of cell death increases dramatically and 99.9% of cells die in just over 1 hour. Increasing the temperature further, increases the rate of cell death.

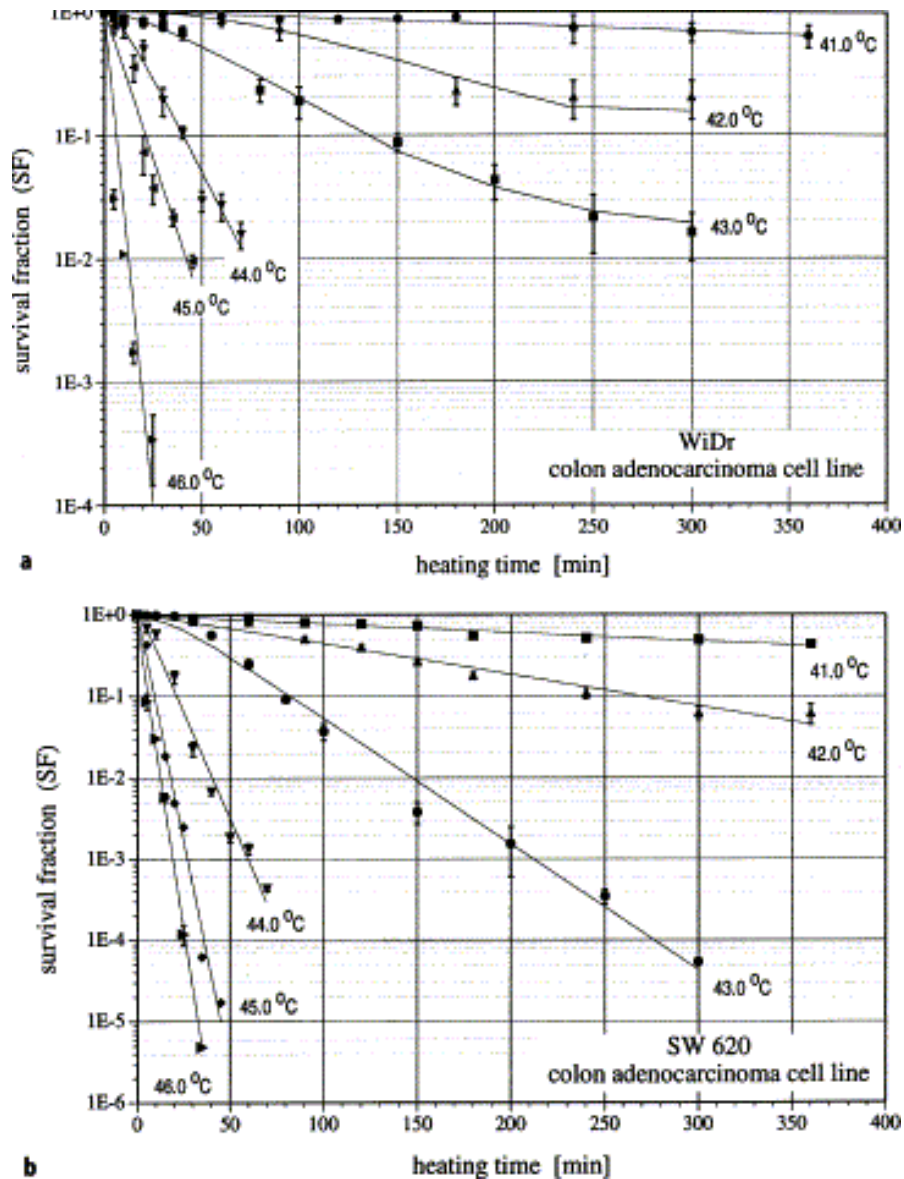


Figure 1. Effect of temperature and time on the survival of different cell lines.¹³

The aforementioned methods in which hyperthermia kills cells can be classified as direct methods. The heat directly injures the cells, and the functionality of these methods relies on a biochemical approach where the thermal energy directly effects the proteins. There are also indirect methods in which hyperthermia kills cells. Heat shock proteins are cells natural defense to experiencing increased temperatures.¹⁷ When a cell experiences higher temperatures it will promote the heat shock protein gene and improve its resistance. This promotion also initiates an immune response which is where the indirect hyperthermal method comes into play. HSP70 (a specific heat shock protein that

prevents apoptosis) expression also induces an anti-tumoral immune response in rats.¹⁸ Triggering this response allows hyperthermia to fight against tumors. Another indirect mechanism relates to the oxygen and nutrient supply of the affected area. Increasing the temperature of the body causes a short term dilation of blood vessels, increase of vascular wall permeability, and an increase in blood flow.¹⁹ These bodily effects result in an increase of nutrient transport across the body. The short term effect of the temperature increase is good for tumors, but prolonged heat has the opposite effect. While the severity depends on the type of tumor, prolonged heat reduces the local blood flow which helps starve it of nutrients. Tumors are more susceptible to the increasing temperature, but other healthy cells may also be affected.^{13,20} Hyperthermia treatment is a multifaceted approach to killing cancer cells.

C. History of Hyperthermia Treatment

Hyperthermia treatments have been around for decades and have had varying degrees of success. The early days of treatment were done as an adjuvant to radiotherapy. In 1990 Datta *et al.* used thermal treatment with a combination of radiation therapy as treatment for patients with head or neck cancer.²¹ The heat was produced from a diathermy unit, which is an external machine that generates heat internally through electromagnetic waves. The treatment was not successful by itself, but when conjoined with the radiotherapy there was a 10% increase in disease free survival when compared to radiotherapy alone. Also concluding in 1990 a Kapp *et al.* researched the effectiveness of heat treatment in combination with radiotherapy in patients with superficial tumors.²² While the heating profile varied, all tumors reached 43°C and were held for 45 minutes. The heating was once again created by an external machine that could target tumors to a moderate degree. This study however found no statistical difference in the effectiveness between radiotherapy and its combination with thermal therapy. Another study in 1990 was conducted by Berdov *et al.* on the combination of thermal and radiotherapy for rectal cancer.²³ They once again used external electromagnetic waves and this time and kept the temperature at 42-43°C for 1 hour. Instead of conducting the radiation and hyperthermal therapy at the same time, this procedure started purely with hyperthermal and after 10 minutes into each session (long enough to reach and be held at temperature)

the radiation commenced. With this treatment regime there was a 20% increase of 5 year survival rates. These early iterations of cancer hyperthermia varied wildly in success, and success was only found when combined with radiation therapy.

Progressing through the 90s many more studies were conducted on the effectiveness of hyperthermia in combination with radiotherapy. In 1993 Valdagni *et al.* with temperatures varying from 41-48°C found a significant increase in 5 year survival.²⁴ Overgaard *et al.* in 1995 found an increase of 28% to 46% in their trials conducted when a tumor temperature of 43°C was held for over 30 minutes.²⁵ Continuing in 1996 Vernon *et al.* used a minimum heat of 43°C for one hour on patients with breast cancer where electromagnetic waves was the heat source. Once again there was a statistical increase, from 41% to 59%, in complete response rates in the patients.²⁶ Sneed *et al.* in 1998 conducted more trials on the effectiveness of hyperthermia in combination with radiotherapy. Observing patients with glioblastoma, an aggressive cancer of the brain, an increase from 15% to 31% was found for 2 year survival in solely radiotherapy versus the combination with hyperthermia respectively.²⁷ The progression through the 1990s led to more conclusive success than the early days. Still the heating methods have limitations based on heating the surrounding healthy tissue, and generally high (above 4°C) temperatures were hard to achieve locally in internal regions. The successes are also marked more on chance of survival through a short time period rather than complete remission of the cancer and total healing of the patient.

Into the 2000s research continued on the usage of hyperthermia in combination with radiotherapy. Van der Zee *et al.* increased the tumor temperature until patients felt pain, and then slightly lowered the heat. While this max temperature varied depending on the patient, the treatment duration only accounted for temperature above 42°C. The 1-1.5 hr hyperthermia therapy was conducted with thermal probes, as the treatment was for pelvic (rectal or cervical) cancer. Complete response rates increased from 39% to 55% when adding the hyperthermia treatment to the radiotherapy.²⁸ In this study the complete response was based on total remission of the tumor, so progress had definitely been made since the earlier days of hyperthermia treatment. Continuing in 2005 Jones *et al.* conducted more research into hyperthermia treatment, once again with superficial tumors being the target. These tumors were heated *via* microwaves and resulted in a complete

response increase from 42% to 66%. A significant increase was observed and here the heat treatment ranged from 43-50°C where lower temperatures had a longer exposure time to compensate.²⁹ Considerable and consistent progress has been made with the hyperthermia treatment, but still it is only being used concurrently with radiotherapy. Even recently in 2015, hyperthermia treatment has been conducted with radiotherapy. Attaluri *et al.* conducted a similar set of experiments to the previous groups but changed the heating source to that of magnetic nanoparticles. This study on rats (to parallel prostate cancer in humans) corroborated what the other methods of heating displayed and there was increased tumor remission.³⁰ While the idea of magnetic hyperthermia has been around for much longer, around 60 years, this study shows that magnetic hyperthermia is still not a mainstream technique for cancer therapies.^{31,32}

D. Magnetic Hyperthermia

Using magnetic particles as the mechanism for hyperthermia is the next logical step for treatment. The older technologies of electromagnetic waves and heat probes had a limited degree of specificity. The control that these technologies did have was also limited by the location of the tumor, with superficial tumors being easier to access. An ideal treatment will be able to specifically target any region of the body and limit denaturation of the surrounding healthy cells. This treatment must also be tunable, so that its temperature can be controlled whilst in the body. With the idea of specificity, both in location and temperature control, magnetic particles becomes a promising choice.³³ Magnetic microspheres are glass particles with elements in it that make it be effected by a magnetic field.³⁴ They can be injected *via* syringe directly into the tumor which completely covers the specificity issue. Magnetic microspheres can also be heated when under the effects of an alternating magnetic field.

The main mechanism of heat generation in magnetic particles in a magnetic field is from the dissipation of magnetic energy. The dissipation is in the form of thermal energy and can come about from three different categories: Eddy loss, hysteresis loss, and relaxation.³⁵ Eddy current is the voltage produced inside a magnetic material when it has an alternating magnetic field acting upon it. Eddy current loss is the loss of energy associated with the current and can be described by the equation:

$$P_e = \frac{kB^2 f^2 d^2}{\rho} \quad (1)$$

where k is a geometric constant, B is the maximum induction, f is the frequency of the magnetic field, d is the smallest dimension transverse to the flux, and ρ is the resistivity.³⁶ The Eddy current loss is not very significant portion for the heat generation in the magnetic particles, but it can also effect surrounding tissue depending on its electrical conductivity.³⁷

Hysteresis loss is the second type of magnetic energy loss mechanism. A hysteresis loop shows the properties of a material depending on the history of the forces that act upon it. For a magnetic hysteresis loop the magnetization depends on the history of the magnetizing force. An example of the typical loop, with magnetic field (H) and magnetization (M), can be seen in Figure 2.

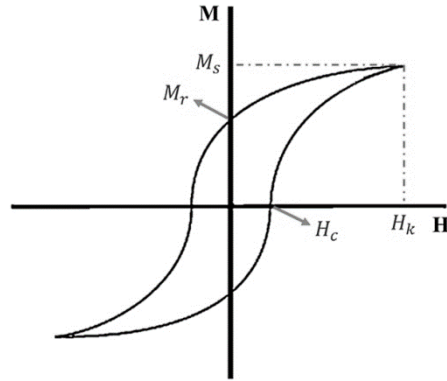


Figure 2. Typical hysteresis loop.³⁵

There are many useful parameters that can be gleaned from a hysteresis loop M_s and H_k relate to the magnetic and field saturation limits respectively, M_r is the magnetization remaining after the field is decreased to zero, and H_c is the magnetic field required to return the magnetization back to zero. The area of the loop relates to the heat loss of the system as can be seen in the following equation:

$$P = \mu_0 f \oint H dM \quad (2)$$

where P is the volumetric power dissipation, μ_0 is the magnetic permeability, and once again f is the frequency of the applied field.³⁵ The power dissipation affects the heat gain of the system, and hysteresis loss is a larger factor than Eddy loss.³⁸ It is also beneficial to note that as the generation of heat relates to the frequency of the field, there is there is a degree of tunability. Being able to control the frequency can control the power dissipation, which will in turn make sure the tumors can stay at the exact temperature required for the hyperthermal therapy.

The third mechanism for temperature gain in magnetic microspheres is from relaxation. Relaxation can either come in the form of Neel or Brownian relaxation. In Neel relaxation the particle has a fixed location and it is the direction of the magnetic moment that rotates with the field, and in Brownian relaxation the magnetic moment direction is fixed with respect to the particle, and the particle moves with respect to the field.³⁵ Figure 3 shows the differences in the magnetic field and superspin direction between Neel and Brownian relaxation.

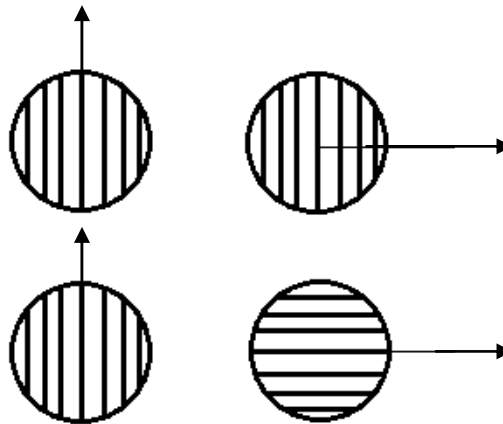


Figure 3. Neel relaxation (above) and Brownian relaxation (below) with the arrow depicting superspin direction.

E. Magnetic Resonance Imaging

Magnetic Resonance Imaging (MRI) is an imaging technique often used in the medical field to distinguish differences between tissues inside the body. It can depict the difference between different tissues, as well as abnormalities within one kind of tissue.³⁹

MRIs work by generating a magnetic field that aligns the dipoles of water in the body. This field is switched allowing for the molecules to relax. MRIs produces very strong magnetic fields (greater than 1.5 Tesla). The alternating magnetic field generates a spin in the nucleus of molecules causing radio waves to be released. These radio waves are detected and analyzed which allows for the differentiation of different types of tissues in the body.⁴⁰ MRI is a well-established technique for identifying tumors, and it can also be just the tool needed to eliminate them. As an MRI generates magnetic fields, it can also be used as the therapeutic tool to generate heat in magnetic hyperthermia treatment. Controlling the frequency of the magnetic field will give control to the materials temperature increase inside the body.

F. Gadolinium

Gadolinium (Gd) is a paramagnetic rare earth element that is commonly used as a contrast agent in MRI. Paramagnetic materials are weakly attracted to magnetic fields based on its unpaired electrons. Paramagnetic materials do not retain the magnetization gained from being in a magnetic field. Contrast agents are serums that are administered to the body before an MRI is conducted. They increase the contrast between different types of tissues so that doctors can have an easier time identifying the differences in tissues. In MRI there are two types of relaxation in water molecules which give distinct signals. T1 is spin-lattice relaxation and T2 is spin-spin relaxation. Contrast agents reduce the relaxation time of both types resulting in a localized increase in contrast between the affected and unaffected tissue.⁴¹ An example of the effectiveness of contrast agents can be seen in Figure 4 where heart tissue has much clearer differentiation after a contrast agent has been administered.⁴² Contrast agents are not always needed, around 30% of MRIs use them, but can be an extraordinary help in the diagnosis process.⁴¹

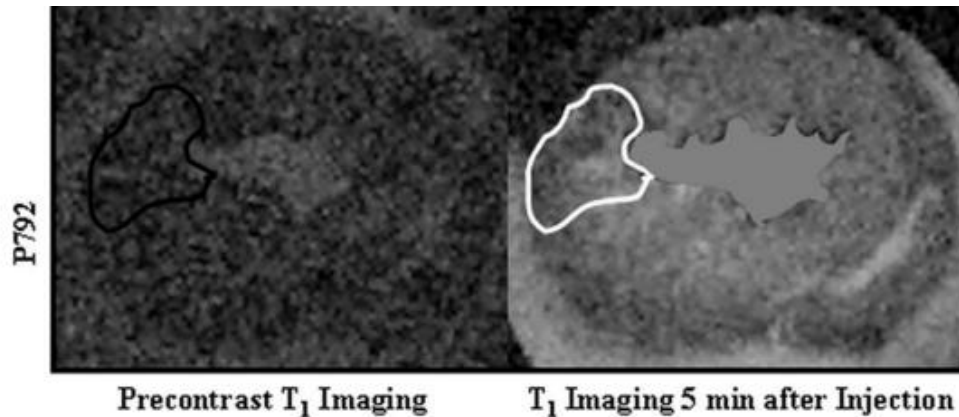


Figure 4. MRI of heart tissue, before and after P792 contrast agent administration.⁴²

Because of the role Gd currently has in contrast agents it is a apt choice for research in hyperthermia. While Gd is currently used in the medical world, it is not without side effects. The main concern in using Gd in the body is for long term kidney problems. Nephrogenic systemic fibrosis (NSF) is an idiopathic, progressive disease⁴³ This means it is contracted spontaneously and worsens over time. There is no effective treatment and it results in moderate to significant disability or even death. NSF occurs in people with kidney or renal diseases and adds on to the existing problem. Symptoms include swelling, itching, and even hardening of the skin, but as it progresses it can cause organ failure. Studies showing the linkage between Gd and NSF caused cautionary steps in 2007. The FDA mandated labels be placed on Gd based contrast agents but did not outlaw them outright. After 2007 more studies were conducted on the safety of these agents, and some studies found little to no association between Gd and NSF.⁴⁴ Others however agreed, and as time elapsed and more data published, the FDA put out another warning including a short list of approved Gd based contrast agents.⁴⁵ GFR represents the amount of blood that passes through the glomeruli (filters of the kidney) in one minute. For perspective, while there is a wide variation, Healthy people tend to have GFRs in the 60-120 mL/min/1.73m² range. After 2007 more studies were conducted on the safety of these agents, and some studies found little to no association between Gd and NSF.⁴⁴ Other studies found Gd depositions inside the brain, even in patients without the associated renal disease.^{46,47} As time elapsed and more data published, the FDA put out

another warning including a short list of approved Gd based contrast agents.⁴⁸ In this new FDA warning it also gave clarification that NSF has only been seen in people with abnormal kidney function, and that risk begins to be associated with a glomerular filtration rate (GFR) of less than 30 mL/min/1.73m².⁴⁹ Gd is only toxic for the body when it is in its ionic form. For typical contrast agents it is chelated and bonded within an organic carrier. This chelation prevents ionic Gd entering the body fluids and organs, however failure of this bonding mechanism can occur which can result in Gd contamination within the body. Using Gd as the heating agent in the microparticles does impart another level of safety consideration for their creation.

G. Holmium

Holmium (Ho), like Gd is a paramagnetic rare earth element. Using Ho as the active heating agent may be a safer alternative to Gd based treatments. While the effects toxicity of Ho is not fully known it is generally safe for the body. While eating or inhaling large amounts of Ho is bad for the body, Ho at 16 ppm in the body results in no toxicity.^{50,51} The safety of Ho makes it an appealing alternative for Gd for hyperthermia treatment. It is not only the safety aspect that makes Ho a good candidate to study in treatment, it is also the most magnetic permeable element.⁵² Ho has been used successfully for imaging in MRI, making it extremely comparable to Gd for studies cancer hyperthermia.⁵¹

H. Iron and Manganese

Iron (Fe) and Manganese (Mn) are transition metals with magnetic properties. Mn, like Gd and Ho, is paramagnetic, and Fe is ferromagnetic. Mn is of interest because of its use as a contrast agent in MRI.⁵³⁻⁵⁵ Mn does not have the same degree of paramagnetism as either Gd or Ho, but it is a good functional element to investigate because of its widespread MRI imaging.⁵⁶ Fe has shown positive results previously in magnetic hyperthermia.³⁷ Even though Fe is typically thought to be the ideal material for magnetic properties, investigating the success of ferromagnetism versus paramagnetism will be useful for understanding the process as a whole. Fe and Mn are essential

elements for the body, but that does not mean they are perfect. In excess amounts Fe can be toxic and even promote tumor growth.^{37,57} Fe and Mn both cause neurodegenerative disorders with Parkinson like syndromes.⁵⁸ Mn also has poor biological implications on its own, and in excess amounts is toxic for male reproductive organs.⁵⁹

I. **Objective**

The primary aim of this thesis is to evaluate the effectiveness and safety of various compositions of glass microspheres for cancer hyperthermia treatment. The most important factor that will determine success is the iron release of the glasses. If a toxic amount of Gd, Ho, Fe, or Mn is released then there is no chance of implementation into the body. Secondary consideration for this work is the physical nature of the spheres. Consistency is crucial in the medical industry, so delivering a highly reproducible product is important for passing clinical trials. The third consideration is understanding the overall structure of the glass. There are many interactions in a 5-component glass system, and knowing what is happening on an atomic level will be useful for making changes to the process.

II. EXPERIMENTAL PROCEDURE

A. Material Synthesis

1. Glass Powder Synthesis

The described glass compositions was synthesized using the traditional melt-quench method where the batched analytical grade reagents (SiO_2 , Gd_2O_3 , CaO , GeO_2 , P_2O_5 , Gd_2O_3 , Ho_2O_3 , Fe_2O_3 , and Mn_2O_3) for each glass composition will be brought above the melting temperature (1500°C) in an alumina crucible and poured in cold water to form glass frit. A glass with a basic starting composition of 30SiO_2 - $10\text{P}_2\text{O}_5$ - 25GeO_2 - 35CaO (mol%) was used for this study. A 5 mol % stepwise substitution of CaO for the experimental reagents (Gd_2O_3 , Ho_2O_3 , Fe_2O_3 , Mn_2O_3) was undertaken until the glass lost its amorphous structure. The resulting 15 compositions and their nomenclature is presented in Table 1. After the quench the resulting glass frit was dried, ground, and sieved to retrieve a glass particle size $<100\mu\text{m}$.

2. Glass Microsphere Synthesis

The glass particles were formed into glass microspheres by introducing the particles into a propane/oxygen flame where they melted and formed a spherical liquid droplet by surface tension. The spheres are cooled as they leave the flame and result in glass microspheres. The flame of the Hellcat torch (Carlisle Machine Works NJ, USA) is directed into a stainless-steel container which collects the glass microspheres as they are expelled from the flame. The inner candles of the flame are kept distinctly to 4cm for each glass composition. Outer oxygen is kept cracked to prevent any backflow, and outer propane is not used.

Table I Naming Convention. Glass nomenclature and Composition of the Glasses

Name	Substituent	CaO	SiO₂	P₂O₅	GeO₂
Control	0	35	30	10	25
5 Gd	5	30	30	10	25
10 Gd	10	25	30	10	25
15 Gd	15	20	30	10	25
20 Gd	20	15	30	10	25
5 Ho	5	30	30	10	25
10 Ho	10	25	30	10	25
15 Ho	15	20	30	10	25
5 Fe	5	30	30	10	25
10 Fe	10	25	30	10	25
15 Fe	15	20	30	10	25
20 Fe	20	15	30	10	25
5 Mn	5	30	30	10	25
10 Mn	10	25	30	10	25
15 Mn	15	20	30	10	25
20 Mn	20	15	30	10	25

B. Glass Powder Characterization

1. X-Ray Diffraction (XRD)

Diffraction patterns were collected using a Siemens D5000 X-ray Diffraction Unit (Bruker AXS Inc., WI, USA). Glass powder samples were packed into standard polymer sample holders. The X-Ray source was CuK_α, and a generator voltage of 40kV and a tube current of 30mA was employed. Diffractograms were collected in the range 10° < 2θ < 70°, at a scan step size of 0.02° and a step time of 1s. Any crystalline phases present were identified using TOPAS.

2. Thermal Analysis

A combined differential thermal analyser, thermal gravimetric analyser, and differential scanning calorimeter (DTA-TGA-DSC) (Stanton Redcroft STA 1640, Rheometric Scientific, Epsom, UK) was used to measure the glass transition temperature (T_g) of the powder. A heating rate of $20^\circ\text{C min}^{-1}$ was employed using an alumina crucible where an empty matched alumina crucible was used as a reference. A starting weight of 20-30mg was used for each sample. Sample measurements were carried out every two seconds between 30°C and 1350°C .

3. X-Ray Photoelectron Spectroscopy (XPS)

High resolution and survey scan X-Ray Photoelectron Spectroscopy (XPS) were conducted with a Kratos AXIS 165 spectrometer (Kratos Analytical, Manchester UK) using monochromatic Al K_α radiation ($h\nu = 1486.6 \text{ eV}$). The C1s peak C-C peak at 284.8eV was used to calibrate the scan. The XPS was performed on the glass powder samples

4. Advanced Surface Area and Porosity (ASAP)

In order to determine the surface area of the glass powder, Advanced Surface Area and Porosimetry, Micromeritics ASAP 2020 (Micromeritics Instrument Corporation, Norcross, USA) was conducted. Approximately 8g of each powder was analyzed, and the specific surface area was calculated using the Brunauer-Emmett-Teller (BET) method.

5. Glass Particle Solubility and Ion Release

Glass particles were immersed in sterile Millipore de-ionized H_2O for 1, 10, 100 and 1000 hours. All time periods were conducted for the Gd samples, while the Ho, Fe, and Mn samples were recorded only at the 1000hr time period. Approximately 0.1 m^2 surface area of particles were submerged in 10 ml of de-ionized H_2O and spun at 40rpm at 37°C . The ion release profile of each glass was measured using Inductively Coupled Plasma – Optical Emission Spectroscopy (ICP – OES) on a Perkin-Elmer Optima 8000 (Perkin Elmer, MA, USA). ICP – OES calibration standards for Si, Ge, Gd, Ho, Fe, and Mn ions were prepared from a stock solution on a gravimetric basis.

C. Glass Microsphere Characterization

1. Optical Microscopy

Determination of the microsphere diameter was conducted using an Olympus IX20-UCB Optical Fluorescent Microscope at 4X magnification. The mean particle diameter was calculated by measuring the microspheres using Image-Pro AMS 5.1 which was calibrated using a 100 μ m calibration standard. A random sample of microspheres was placed on a glass slide and 30 individual microspheres were measured.

2. Corrosion Study

Solutions of pH 4, 7, and 10 (± 0.02) were made using DI water, NaOH and HCl. A calibrated Corning 430 pH meter was used to determine the pH. Spheres were placed into each solution for 1, 10, 100, and 1000 hours. 1.5 mL of solution and 10 mg of spheres were added to a microcentrifuge tube, shaken once, and then kept stationary at 37°C for their respective time periods. After the allotted time the spheres were washed with DI water and returned to the incubator for the liquid to evaporate.

3. Scanning Electron Microscopy (SEM) and Energy Dispersive X-Ray Analysis (EDX)

Backscattered electron (BSE), and secondary electron (SE) analysis was carried out with an FEI Co. Quanta 200F Environmental Scanning Electron Microscope. Samples were gold coated prior to imaging. Images were taken at 8kV and with a spot size of 3. Additional compositional analysis was performed with an EDAX Genesis Energy-Dispersive Spectrometer (EDS). All EDS spectra were collected at 15 kV for 50 s with a spot size of 4. Quantitative EDS spectra were subsequently converted into relative concentration data.

III. RESULTS AND DISCUSSION

A. Glass Powder Characterization

1. X-Ray Diffraction (XRD)

Initial glass characterization included x-ray diffraction and the resulting patterns obtained from the glass ceramics can be seen in Figure 5 and Figure 6. The control composition has the characteristic amorphous hump of a glassy material, as well as crystalline calcium phosphate peaks. These distinct peaks show that the material is a semi-crystalline glass-ceramic. When increasing concentrations of Gd are added and Ca are removed, the degree of crystallinity increases. The increase in crystallinity also comes with a shift in the structure of the lattice. It evolves from being a glass with CaPO₄ crystals to glass with CaGdPO₄ crystals. The crystal lattice of the Gd sample was found to be cubic (ICD: 04-006-9035). Holmium (Ho) samples follow a similar trend, the more Ho added, the more crystalline the sample becomes. In this case the transition is to holmium phosphate. The 15 Ho sample was found to be highly crystalline and only displays a small amorphous hump. The Ho lattice was found to be tetragonal (ICDD: 04-006-7940). The iron (Fe) and manganese (Mn) samples deviate from the Gd and Ho samples. With these samples the amorphous humps broaden with increasing concentration of the substituent. With the Fe samples there is still the trend of the substituent being added to the crystalline lattice, so in this case FeCaPO₄. There is little to no evidence of this phase when reaching the higher concentration samples, 15 Fe and 20 Fe. The iron samples were found to be hexagonal (ICDD: 00-045-0338). For the Mn samples only the CaPO₄ peaks associated with the control sample exist and they completely diminish by the 20 Mn sample. This bravais lattice was found to be orthorhombic (ICDD: 00-009-0348). A crystalline structure is beneficial for the microspheres. Ion release is reduced when there is an increase in crystallinity.⁶⁰⁻⁶² The atomic structure of the glass is promising for the success of the glasses use in the body.

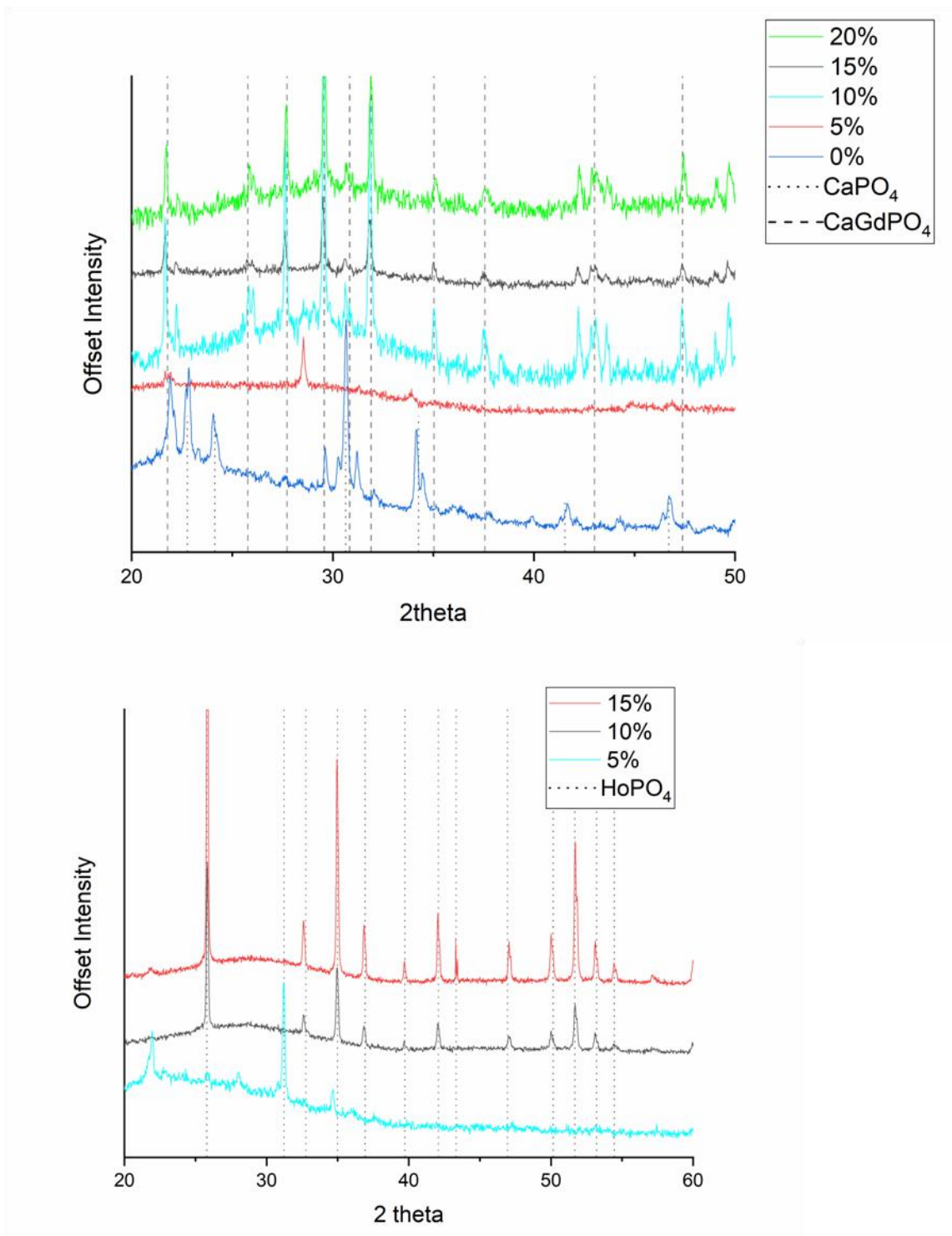


Figure 5. X-Ray Diffraction patterns of glass powder samples. Top: Gd and bottom: Ho.

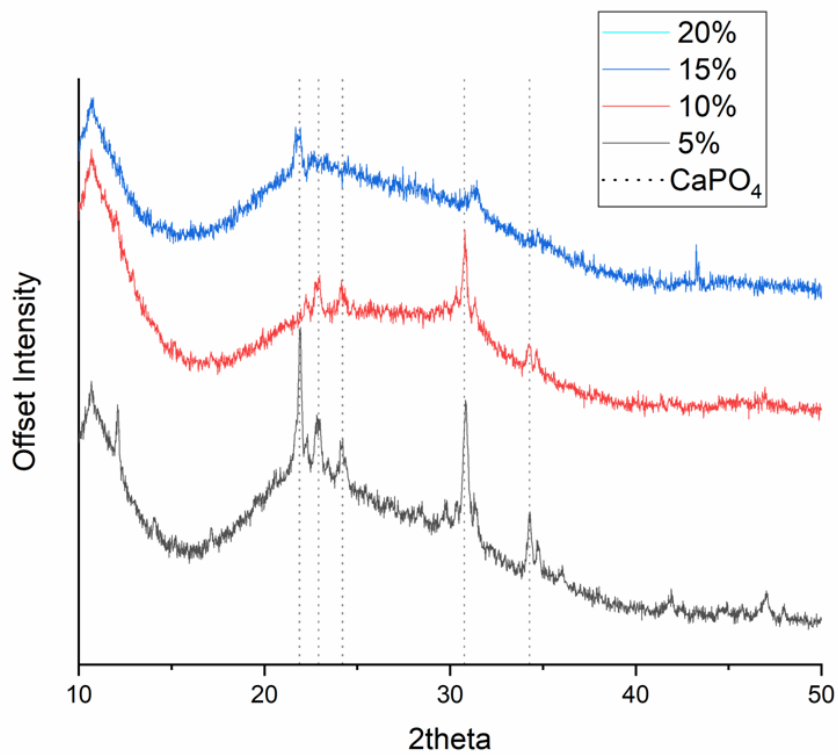
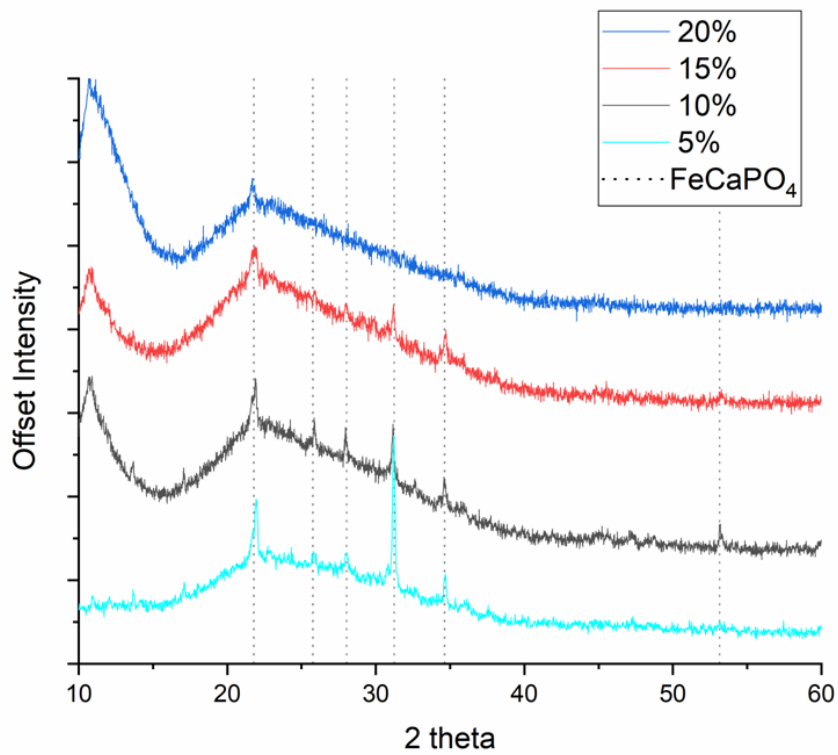


Figure 6. X-Ray Diffraction patterns of glass powder samples. Top Fe and bottom: Mn.

Based on the XRD data it is clear that the samples range from glass-ceramic to glass. Fe and Mn act as glass modifiers which should be seen in the thermal data to lower the melting and glass transition temperatures. Ho plays the opposite roll and should be seen increasing these temperatures making it harder to super-cool. The Gd samples are less clear as there is always a similar degree of crystallinity.

2. Thermal Analysis

DSC and DTA results are presented in Figure 7 and depict trends based on composition. For Gd, the heat flow increases with an increase in Gd composition, while an increase in Ho concentration decreases the heat flow. There is no noticeable trend for the Mn and Fe samples. The temperature difference curves exhibit the same trends or lack thereof for all samples. The temperature stayed within 2.5°C of the empty reference pan. Crystallization occurred in the Gd and Ho samples at 1050°C and the 10 and 20 Gd samples and the 10 Ho sample depicted the greatest peak in crystallization.

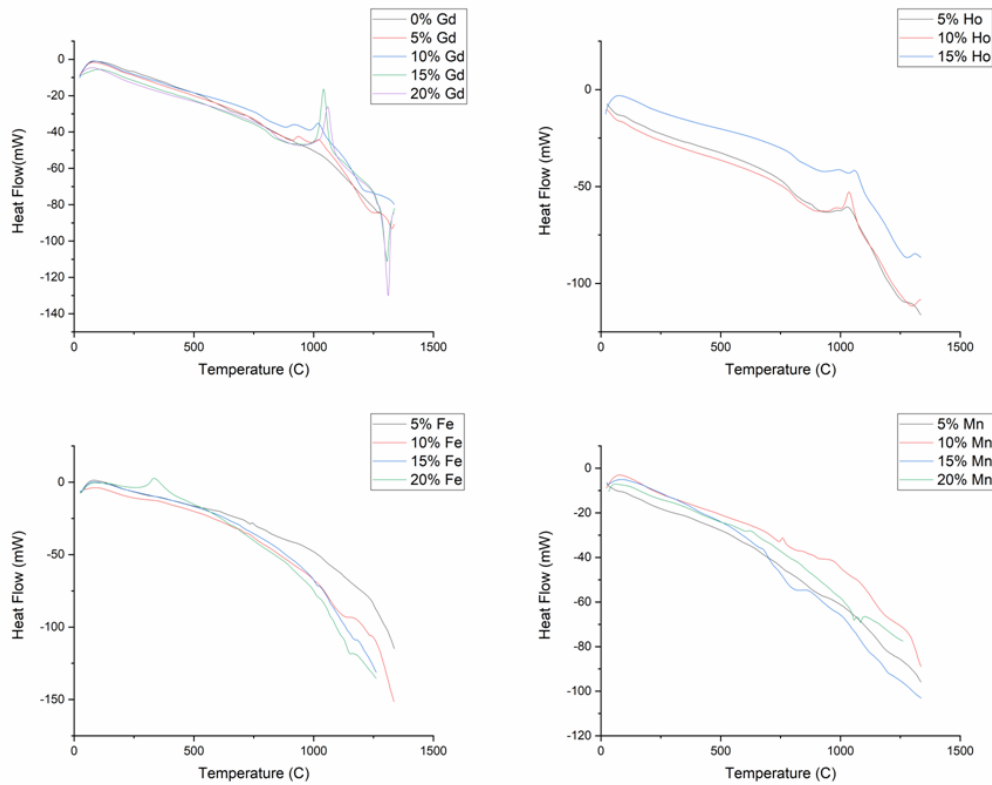


Figure 7. Heat flow curves from glass powders.

The glass transition temperature (T_g) was found by locating the first change in concavity above 400°C on the heat flow curve. Based on the heating rate of 20 °C/min, the T_g does not have a high degree of accuracy, as such the values are only reasonably accurate to $\pm 5^\circ\text{C}$. The glass transition temperatures can be seen in Figure 8 and Table II. The Gd and Ho had the highest T_g and Mn and Fe had the lowest. There was a decrease in T_g when increasing the substituent composition, regardless of the substituent. The exception is that the 20 Gd had a higher T_g than 15 Gd and 10 Fe had a similar T_g to that of 5 Fe. Exchanging Mn for Ca in a silicate glass network has previously found to reduce the T_g of glasses.⁶³

Gd has been found to be a network former in glass systems⁶⁴⁻⁶⁷, but it can also act as a modifier.^{68,69} The role of Gd depends on the system, so it can be classified as a network intermediate. Ho can be found as a network former.^{70,71} Iron, like Gd is found to be a network former^{72,73} and modifier^{72,74} with Fe^{2+} being the modifier while Fe^{3+} is the former. Mn is found to be a former.^{75,76} Based on the thermal data a definitive conclusion on the elements role in the glass network cannot be drawn.

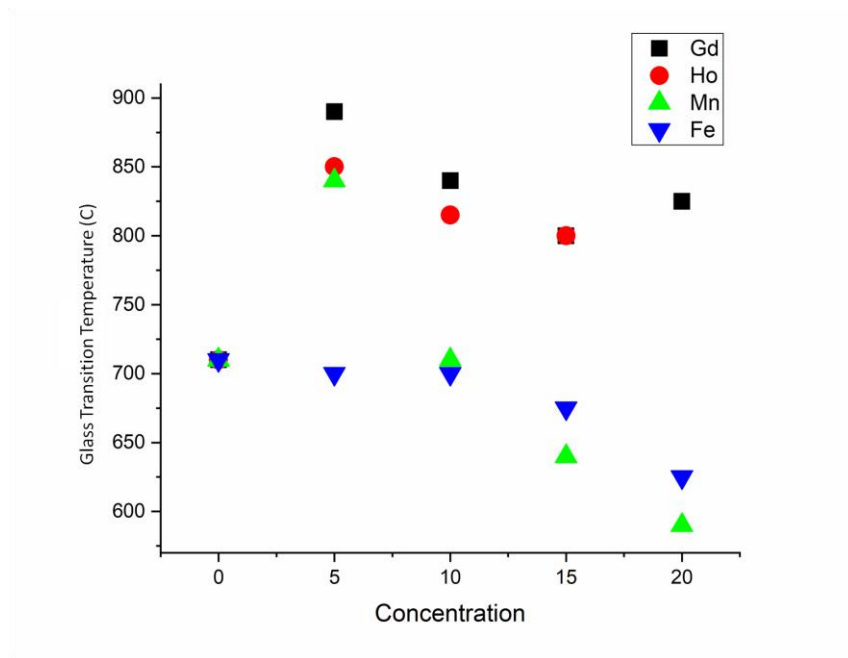


Figure 8. Glass transition temperatures of glass powders.

Table II Glass Transition Temperatures of Glass Powders

Sample	Glass Transition Temperature
Control	850
5 Gd	890
10 Gd	840
15 Gd	800
20 Gd	825
5 Ho	850
10 Ho	815
15 Ho	800
5 Fe	700
10 Fe	700
15 Fe	675
20 Fe	625
5 Mn	840
10 Mn	710
15 Mn	640
20 Mn	590

Based on the lowering of the T_g the addition of the substituent seems to have a flux effect on the glass. This is unexpected as it is removing Ca from the network which is known to be a flux.⁷⁷ The Mn series displays the largest change in T_g and results in the lowest overall T_g of 590 °C. Lower glass transition temperatures result in easier microsphere creation so based on the thermal analysis the 15 Gd, 20 Ho, 20 Fe, and 20 Mn should have the best efficiency and lowest required flame temperature to create spheres.

3. X-Ray Photoelectron Spectroscopy (XPS)

The XPS survey scans for all glass powder compositions can be seen in Figure 9- Figure 12. The O s1 peak at 534 eV was used to evaluate the ratio of bridging oxygen

(BO) to non-bridging oxygen (NBO). The sharp peak at 350 eV is for Ge 2p3, 190 eV for P 2S and 105 for Si 2p. The peak at 347 eV for Ca 2p decreased with increasing substituting concentration which follows the removal of calcium during batching to account for the substituent. Qualitatively the survey scan accounts for each element in batching.

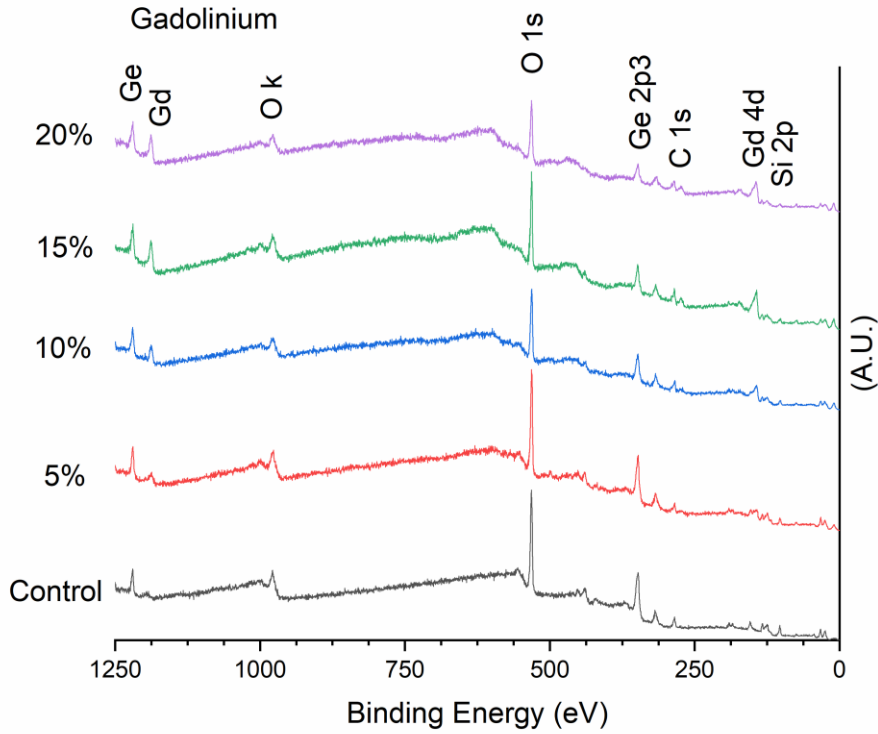


Figure 9. Survey XPS scans for Gd glass powders.

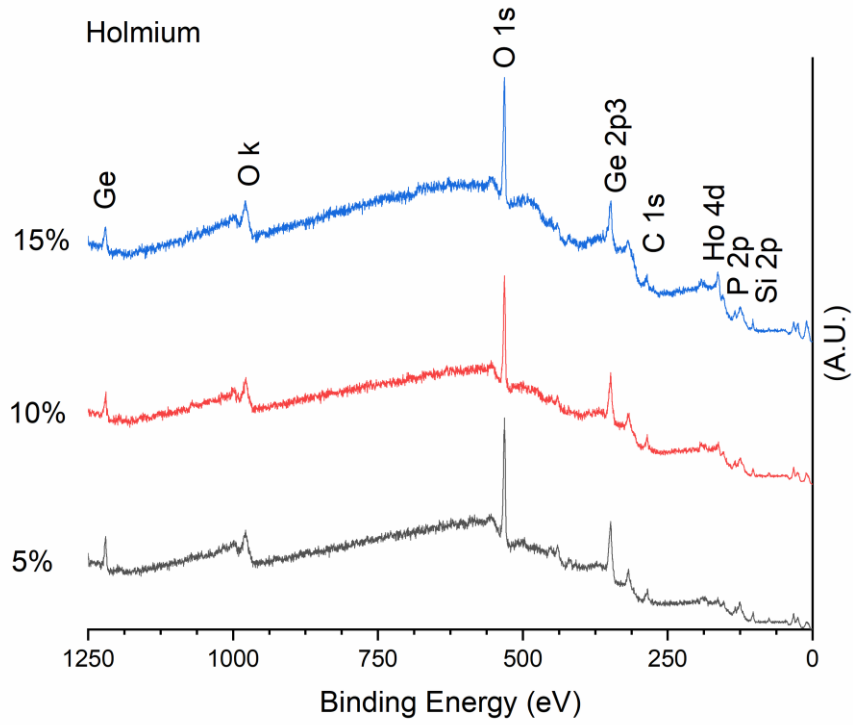


Figure 10. Survey XPS scans for Ho glass powders.

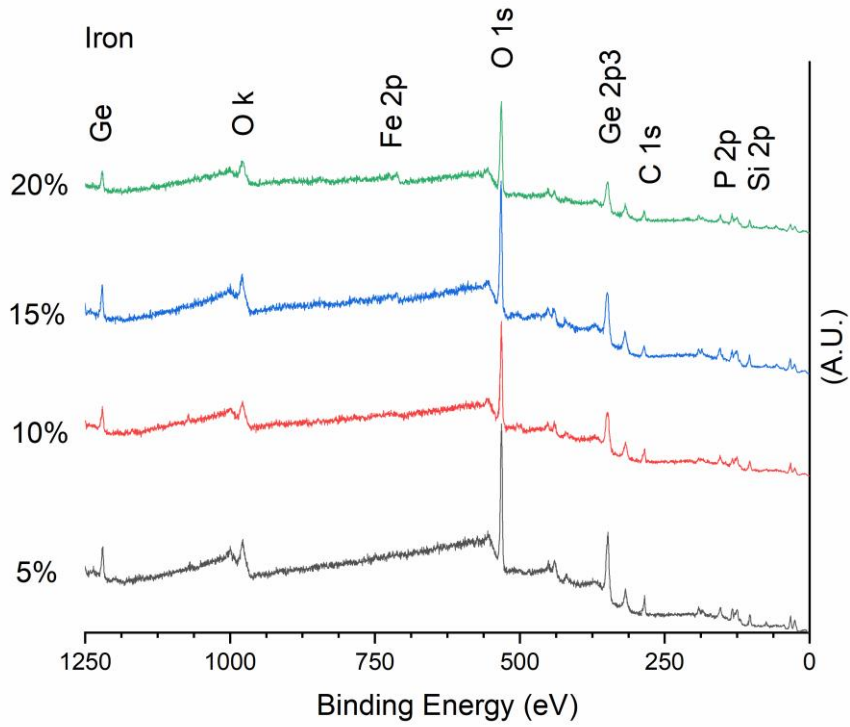


Figure 11. Survey XPS scans for Fe glass powders.

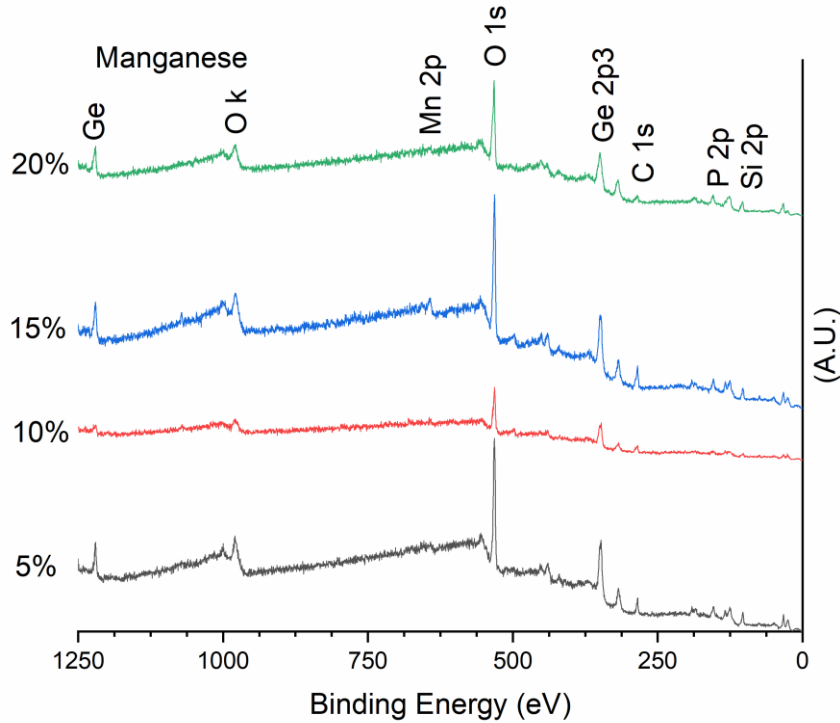


Figure 12. Survey XPS scans for Mn glass powders.

Quantitative analysis was conducted on the high-resolution O 1s peak using OriginLab software. A Gaussian fit was given to both peaks located as a part of the O 1s peak. A linear background noise function was subtracted from the area integration, and the fittings for the Gd samples O 1s can be seen in Figure 13. The peak located at 531.5 eV is for the NBO and the peak at 533 eV is the BO peak. The higher energy peak relates to Si-O-Si bonds.^{78,79} The percentage of oxygen found in the BO and NBO state for all compositions can be found in Table III. There are a lot of compositional factors that contribute to these peaks, so it is difficult to draw conclusions on the significance of each element's contribution to these peaks. Network formers such as Si add to the concentration of BO in the sample, however Ge (can exhibit 6-fold coordination) and P (can exhibit many different coordination types) add to the NBO peak. The levels of NBO calculated are likely higher than the bulk sample. The high crystallinity of the glass from the XRD and the low levels of ion release both suggest a secure glass network with lots of bridging oxygen. In a Li₂O-Al₂O₃-GeO₂-P₂O₅ glass system there was Ge with octahedral and P with tetrahedral coordination. This system resulted in around 50% NBO

and BO.⁸⁰ Another study found decreasing the Ge content of a Na₂O–CeO₂–GeO₂ decreased the ratio of NBO to BO in the glass system.⁸¹ Ge can also be found as tetrahedra in glasses which further complicates evaluating its overall effect on the NBO levels.⁸² The increasing Ho concentration resulting in a slight increase in NBO as seen in Figure 14, can be simply related to the decrease in Ca which decreases the fluidity of the glass matrix. Using this explanation however is contradictory to the decrease in NBO with increasing Gd concentration, and completely ignores the changing effect of Fe and Mn on the NBO content. Gd has been found to decrease, then increase the levels of NBO in a borate glass system, which does corroborate the data achieved here.⁶⁸ With this in mind the largest conclusion that can be drawn is that the substituent concentration only has a moderate effect on the total structure of the system. While the XPS analysis shows that the NBO content ranges from 70-93% for all samples, there must be a different explanation for the location and shift of these peaks. Future analysis on the effect a complex network has on the oxygen's binding energy in any glass system will allow for a better understanding of the NBO levels in this glass.

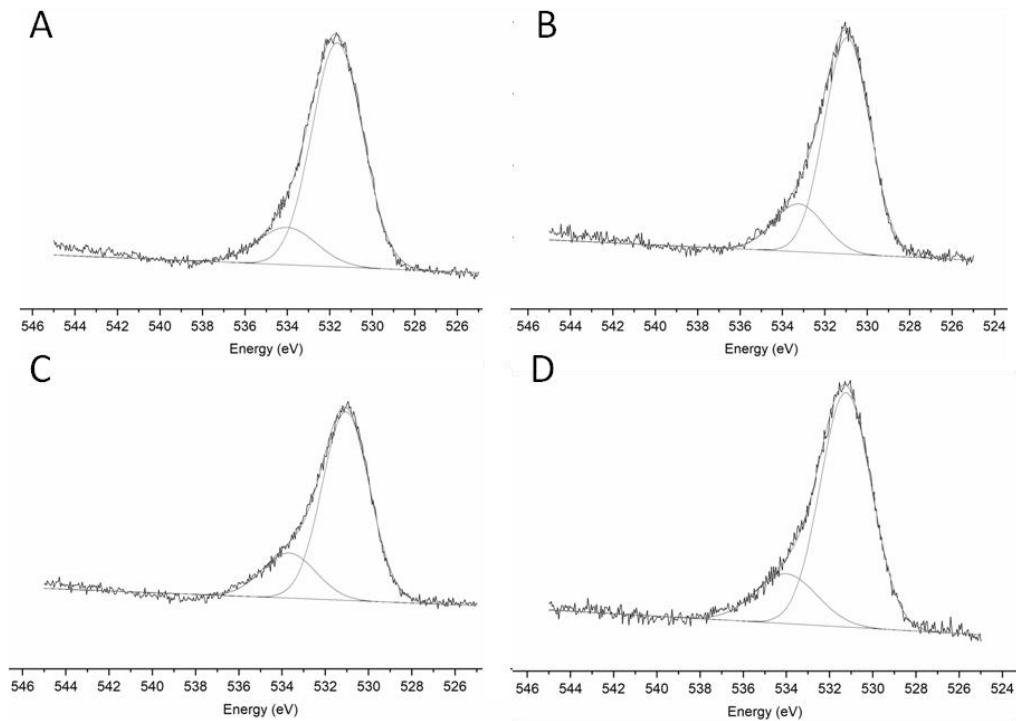


Figure 13. High resolution XPS for Gd glass powder. A: 5%, B: 10%, C:15%, and D: 20%.

Table III Bonding and Non-Bonding Oxygen levels for Glass Powder Samples

	Non-Bridging Oxygen (%)	Bridging Oxygen (%)
Control	87	13
5 Gd	84	16
10 Gd	80	20
15 Gd	79	21
20 Gd	80	20
5 Ho	89	11
10 Ho	90	10
15 Ho	90	10
5 Fe	93	7
10 Fe	74	26
15 Fe	84	16
20 Fe	87	13
5 Mn	90	10
10 Mn	73	27
15 Mn	86	14
20 Mn	70	30

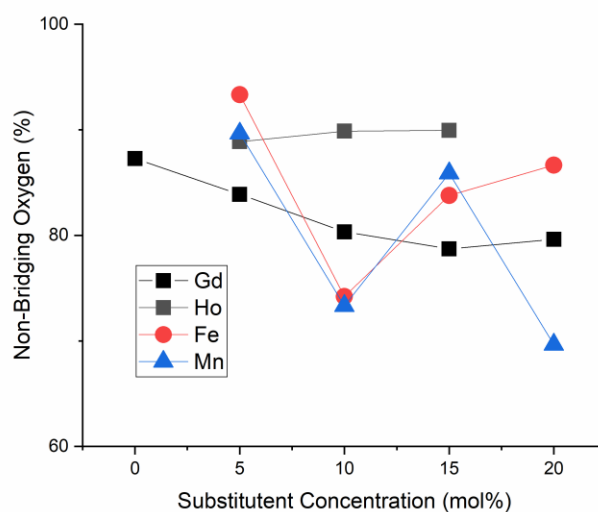


Figure 14. NBO content as a function of substituent concentration.

B. Glass Corrosion Studies

1. Glass Particle Solubility and Ion Release

Ion release profiles were determined for the Gd samples at 1, 10, 100, and 1000 hr. The ions that were analyzed for these samples were the Gd^{2+} , Si^{4+} , and Ge^{4+} ions and their release can be observed in Figure 15. ICP-OES, demonstrated that there was effectively no (less than 0.015 ppm) Gd release over any of the time periods. The 20 Gd sample had the most Gd release, but being that all release was well below sub ppm the samples release rates were effectively the same. Gd was analyzed because any Gd release can incur toxicity within the body. The median lethal dose for Gd is 100-200ppm, so these glasses described are well within a safe limit at 1000 hr.⁸³ These glasses are designed to be bioinert and remain within the body, low Gd release is crucial. Si release was also recorded as its release can be used to represent the breaking of the glass network (Si-O-Si). Similar to the Gd, the Si release was low, sub 10ppm for all samples, and the control and 5 Gd sample with 6 and 8 ppm respectively. This level of Si release is lower than that of the a similar glass microsphere system.⁸⁴ Ge was analyzed for the same reason as the Si, and presented similar results. This time the control and 5 Gd samples had presented over 20-50 ppm respectively. The other samples were much

lower and remained around 6 ppm for all time periods. The control samples had high levels of deviation ranging from 50-250 ppm over the timeframe.

An ion release study was also conducted on all the glass powders at 1000 hr, and the substituent ion concentration, Si^{4+} , and Ge^{4+} can be seen in D, E, and F of Figure 15. In terms of substituent release, Ho was exactly comparable to Gd, and both are very promising for being safe for the body. The 5 and 10 Mn samples were both excellent releasing essentially 0 ppm over the 1000 hrs, but the 15 and 20 Mn samples showed a much higher degree reaching over 100 ppm for the timescale. All the Fe samples stayed consistent at around 10 ppm. The substituent concentration shows that the 15 and 20 Mn samples are not worth pursuing further as they will not be safe for the body. For Si ion release Ho displayed the same as Gd where increasing substituent ion decreased the amount of Si release. The 5 Ho however released 75ppm, well above the 6 of 10 and 15 Ho. This suggests that the 5 Ho sample is undergoing more degradation and is more susceptible to Ho release at later time points. the Fe and Mn samples both had high levels of release except for the 10 Mn. Once again, these samples look like less attractive choices for the body. The exact same trends are seen for the Ge release as the Si release. Based on the ion release profiles the best choices for the body are 10, 15, 20 Gd, 10, 15 Ho, and 10 Mn. Gd and Mn contrast agents have been found to have a 10% release of their metallic components over just 10 days.⁸⁵ Other Gd based contrast agents release 5ppm over 5 hours.⁸⁶ Iron containing silicate glasses have been found to leach 4ppm of iron every day.⁸⁷

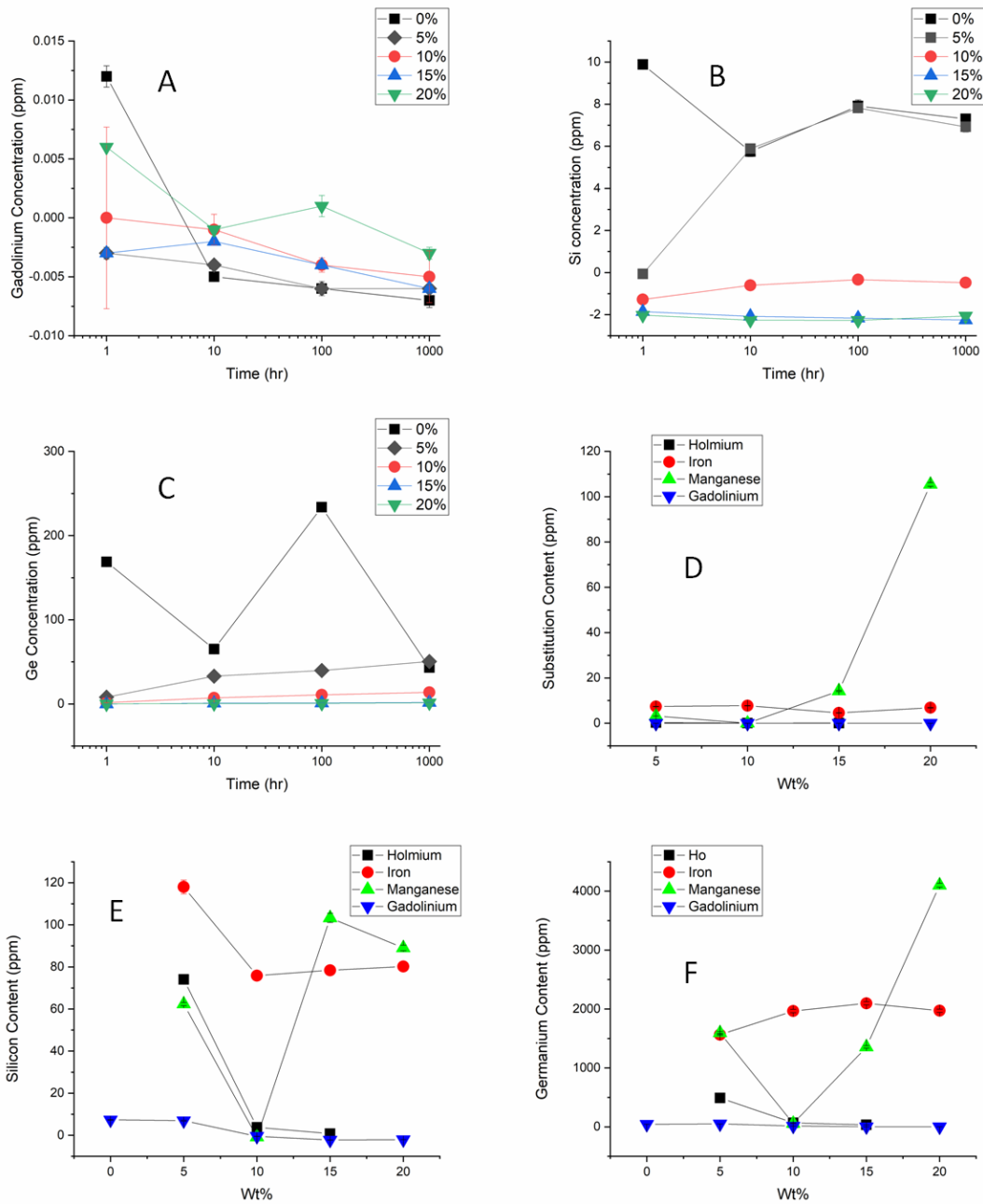


Figure 15 Ion release of Gd powder samples at 1, 10, 100, and 1000 hr: A: Gd, B:Si, and C: Ge, and Ion release of all glass powder samples at 1000 hr: A: Substituent, B:Si, and C: Ge

C. Glass Microsphere Characterization

1. Optical Microscopy

The diameter for each glass microsphere for each composition ranged from 72 to 131 μm , with standard deviations ranging from 8 to 42 μm . The average across all samples was 95.6 μm . The implication with reporting a singular diameter number is that the spherization process was successful and that the resultant was spheres. The size of the spheres can be observed in Figure 16. Reflectance microscopy images of all the spheres can be seen in Figure 17. The majority of the samples had a sphere diameter of 90 μm , but there is no observable trend based on the change in glass composition. As some properties of microspheres come from the T_g , the microsphere diameters were also plotted as a function of glass transition temperature, which can be seen in Figure 18. Once again there was no correlation observed, so the particle size of the end spheres is not based T_g . It is likely that the variation between sphere diameters comes from particle size variations in the original glass powder.

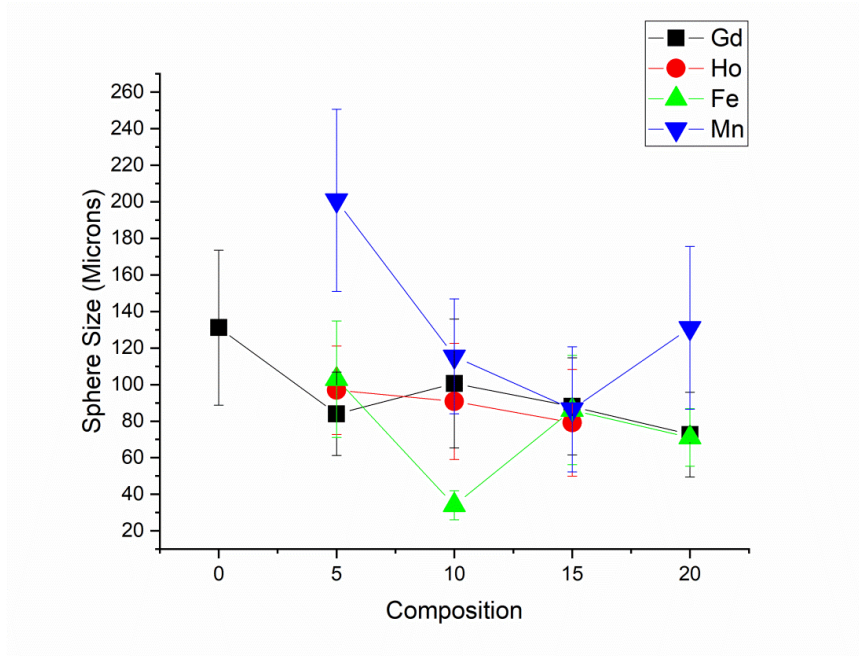


Figure 16. Particle diameter of glass microspheres based on the composition.

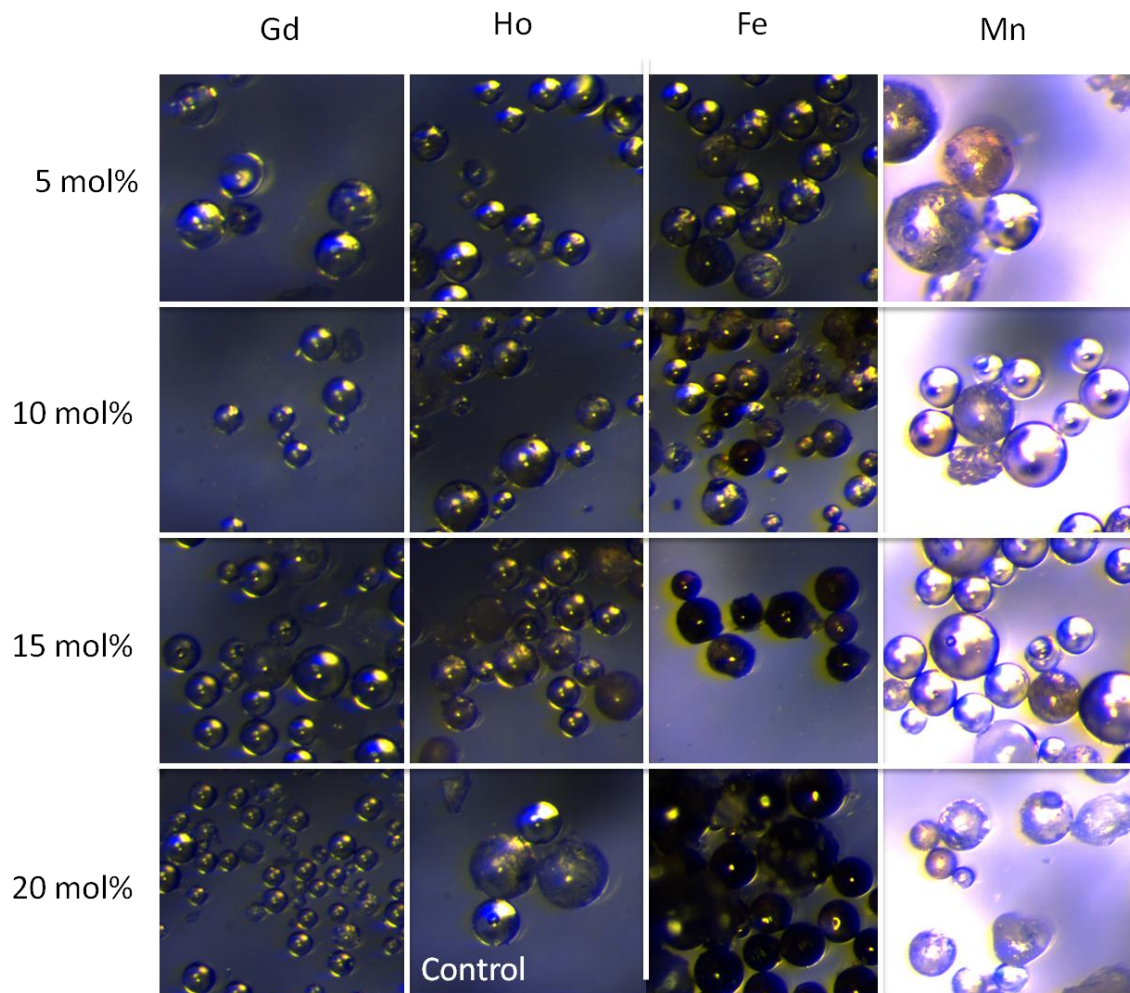


Figure 17. Reflectance microscopy images of all compositions of microspheres.

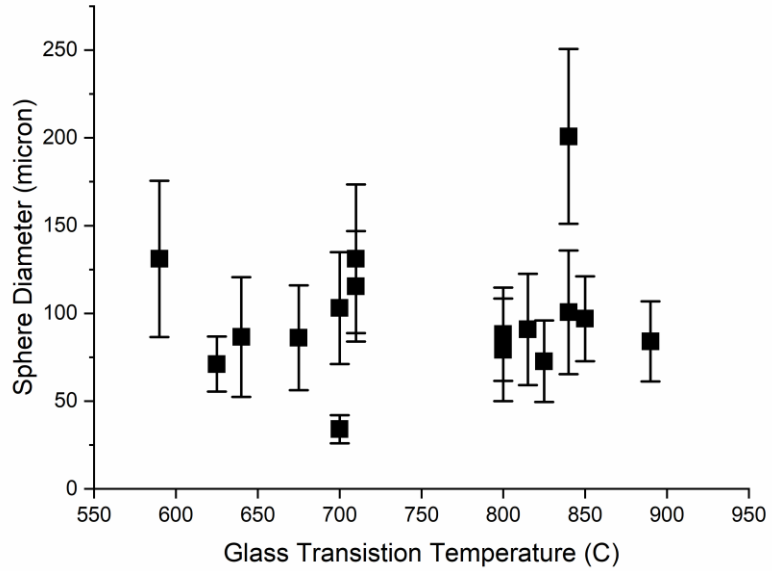


Figure 18. Diameter of glass microspheres based on the glass transition temperature.

While there was a large yield of microspheres in the majority of the compositions, some were less successful than others. There was also an issue with small particles of glass frit sticking to the surfaces of the spheres. A pristine subset of spheres can be seen in Figure 19, while a more tarnished subset can be presented in Figure 20. The consistency in microspheres would need a second step of processing to separate the desired size and to ensure the microsphere shape.

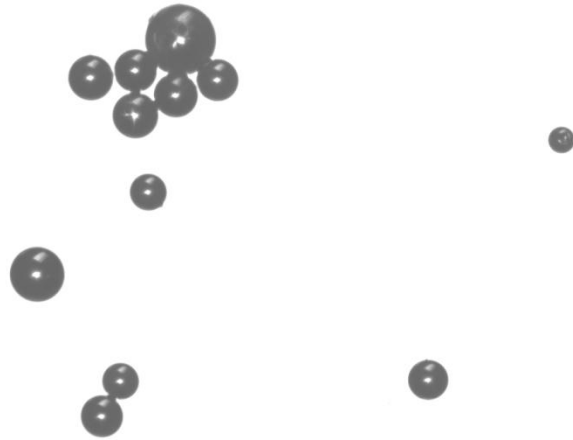


Figure 19. Optical transmission microscopy of 15 Gd microspheres.

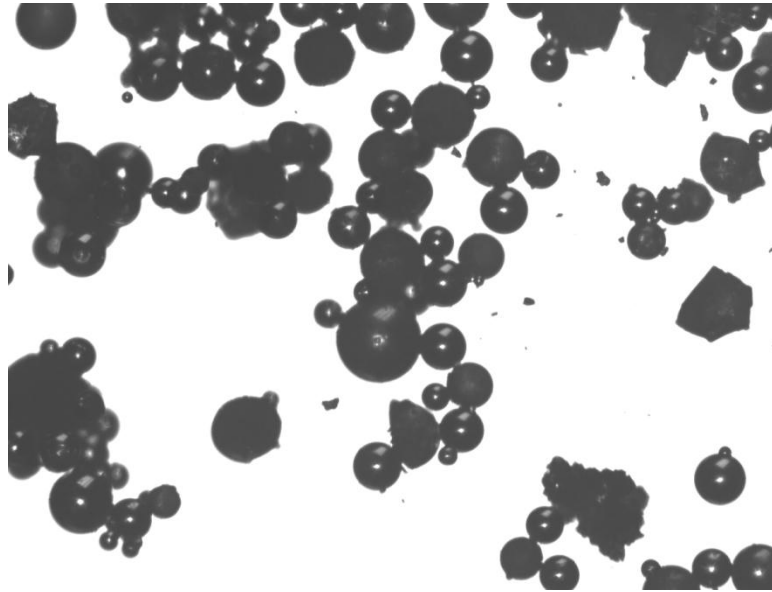


Figure 20. Optical transmission microscopy of 15 Ho microspheres.

2. Corrosion Study

Through 100 hours no corrosion was observed on any of the microsphere's surfaces.

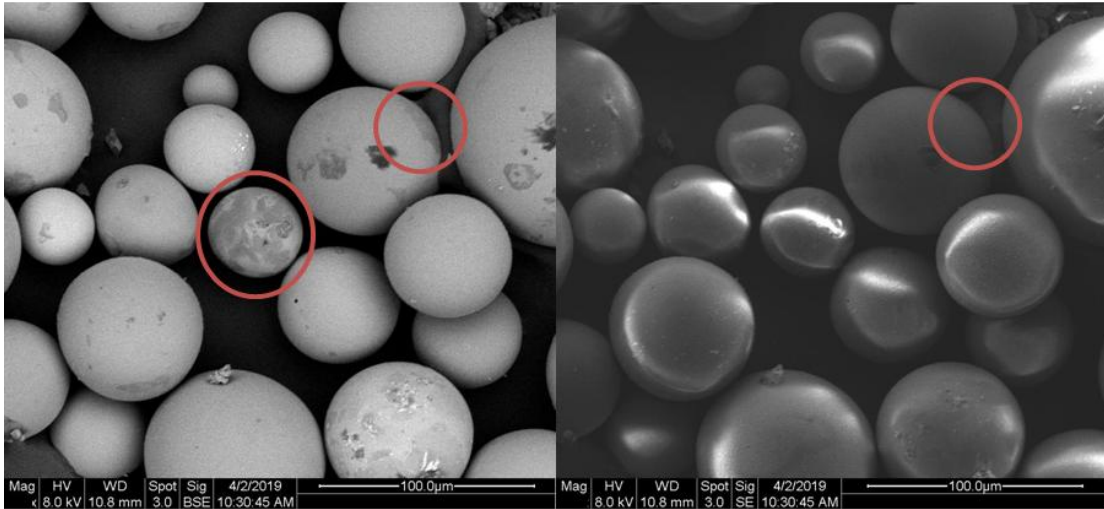


Figure 21 shows evidence of corrosion based on the surface texture of the microsphere in the BSE view, but not in the SE view. Most of the spheres are consistent in SE imaging so the surface texture is an indication of a local change in composition. The other discoloration that could be designated as corrosion is slightly observed in SE mode, so it is likely due to a slight imperfection of sphere shape. This corrosion was seen in a pH 4 solution and did not affect a large subset of surrounding spheres. More evidence of corrosion was evident in a pH 4 solution, but once again it was still an isolated case in the midst of un-corroded spheres.

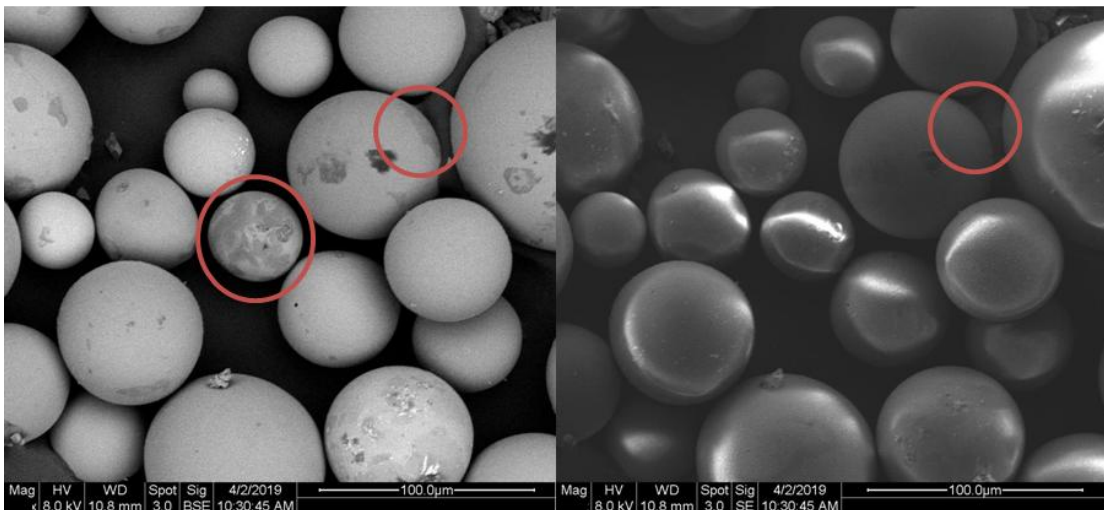


Figure 21. SEM image of 5 Ho spheres after 100 hours in a pH 4 solution. Left and right SE

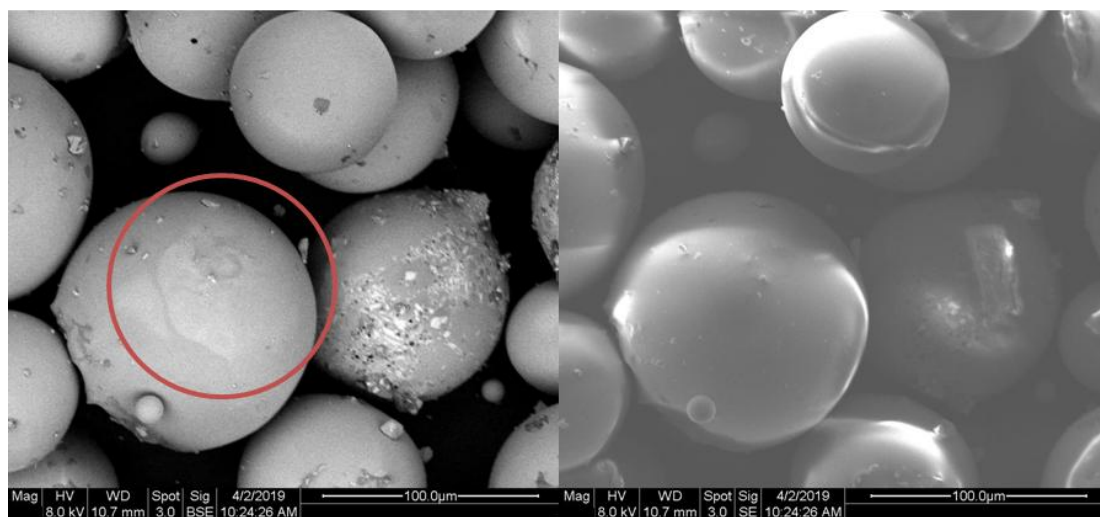


Figure 22. SEM image of 15 Ho spheres after 100 hours in a pH 4 solution. Left BSE and right SE.

Through 1000 hr there was evidence of corrosion, but it was still located primarily with the pH 4 samples. Through 1000 hrs there was different evidence of corrosion seen as branched lattice systems. An example of this can be seen in Figure 23 with the 15 Gd sample. This corrosion was also found in 20 Gd and 15 Ho samples, but not in any of the lower mol% substituent spheres. Even though for the most part the 7 and 10 pH samples did not have evidence of corrosion, there was one type seen at 1000 hr for all three pHs. A roughness, as seen in Figure 24, was developed on the surface of some of the spheres. While it did happen at all pHs the effect was more common, and severe on pH 4 samples. For contrast agents an acid environment has been previously found to release more Gd.⁸⁸ Roughness was also found on samples of all substituent concentrations. Even though more defects were found in the 1000 hr samples they were still not typical overall. While corrosion of the spheres does occur in predictable fashion, it happens at a slow rate.

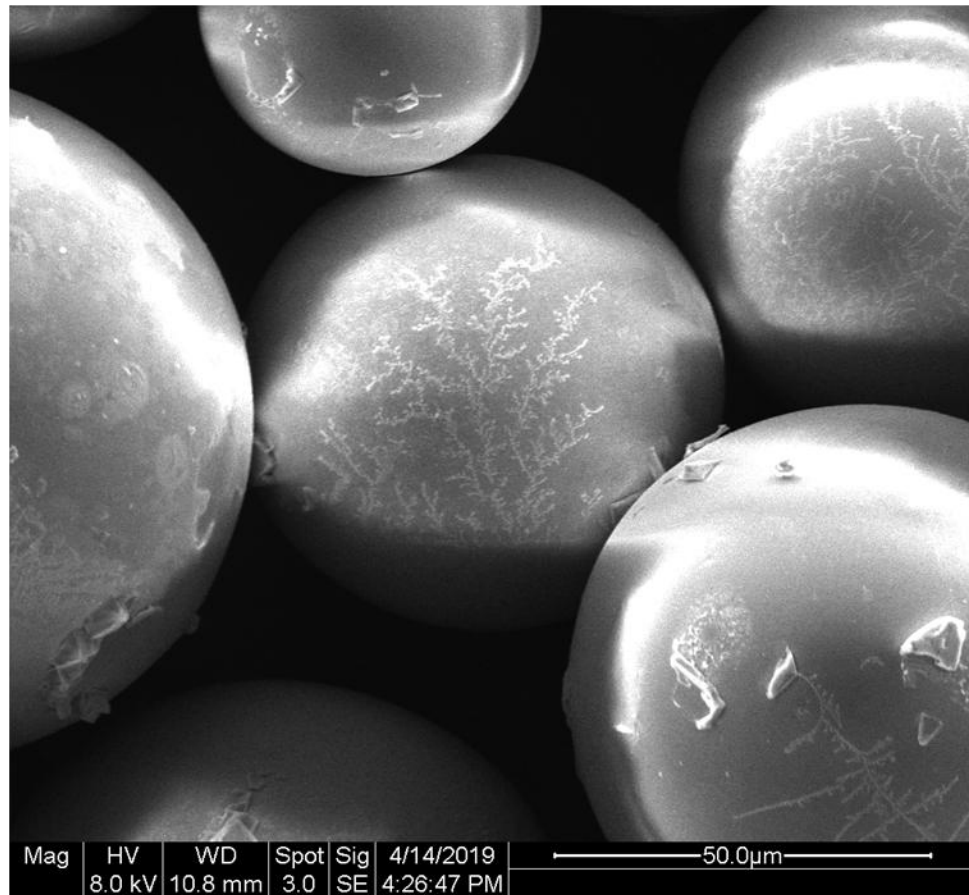


Figure 23 Lattice corrosion of 15 Gd glass microsphere after 1000 hr in pH 4 solution.

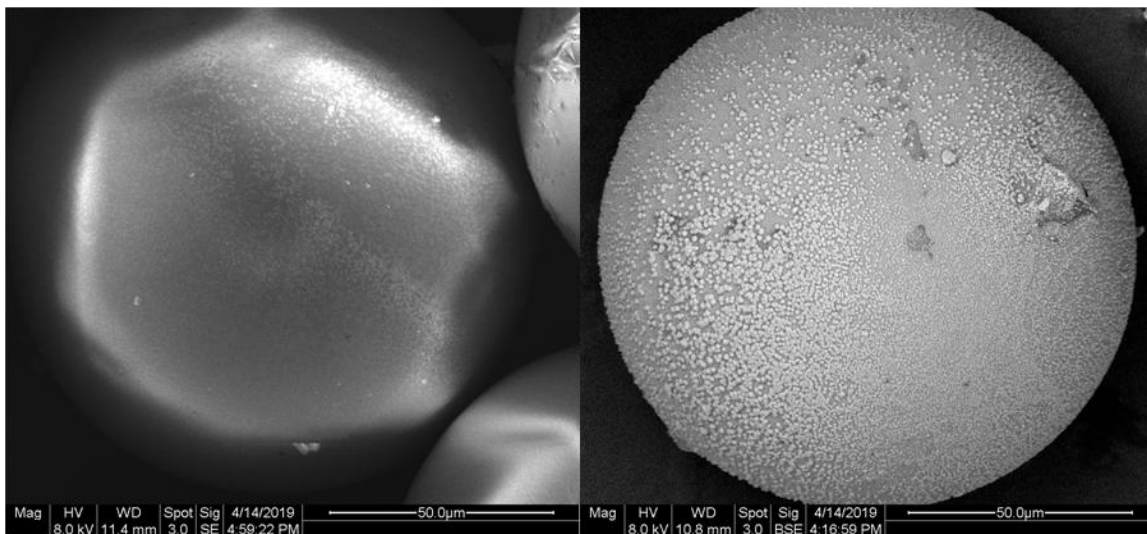


Figure 24 Surface roughness after 1000 hr in solution: left 5 Ho pH 10, right 5 Gd pH 4.

3. Scanning Electron Microscopy (SEM) and Energy Dispersive X-Ray Analysis (EDX)

Visual and compositional analyses were conducted on the glass microspheres after production. The spherical nature of the Gd spheres can be seen in Figure 25. Compositional analysis was done complementarily to the XPS to ensure that the substitutional groups of the powder made it successfully through the microsphere processing. EDX is less quantitative than XPS but it is still a valuable tool for a broad view of the composition of the sphere. Figure 26 shows the linearly increasing concentration of the substituent element with respect to the amount added during batching. This relationship is expected as the more of the ions added, the more is expected within the microsphere, but it is valuable to note that the processing of the microsphere does not result in unexpected changes in composition. EDX analysis did however also show the incorporation of Al in most of the samples. This inclusion was not detected at all on the XPS spectrum which can mean one of two things. XPS only measures around the top 5nm of the surface while EDX measure well into the top 10-200µm of the sample. So either the alumina was hidden in the core of all the powder, and incorporated from the crucible used in melting, or a alumina from the sample holder was detected during imaging.

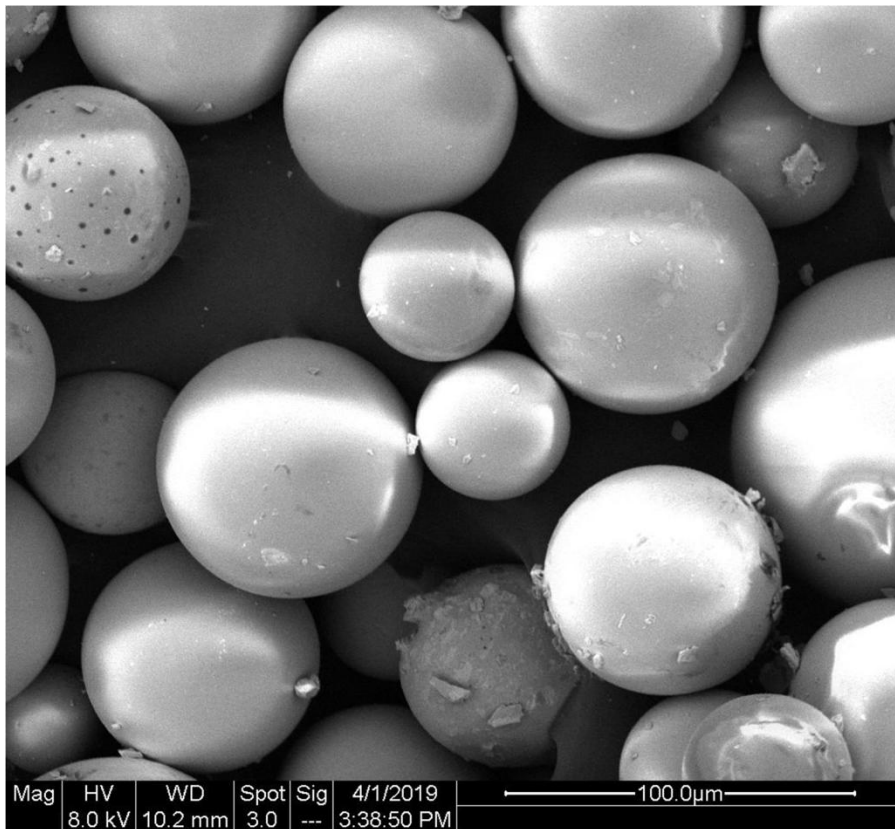


Figure 25. Gd microspheres after production.

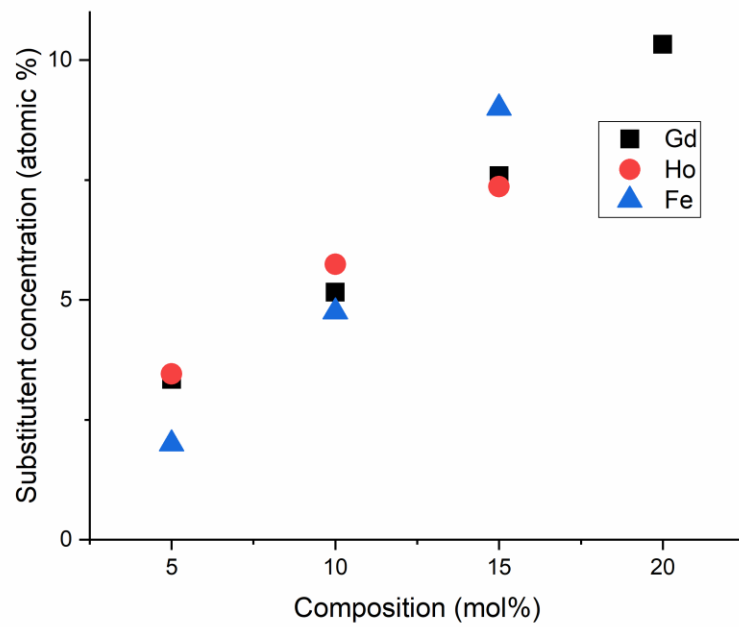


Figure 26. Atomic concentration of substitute in glass microspheres.

EDX elemental maps of the spheres before and after 1000 hr in the pH 7 environment can be seen in Figure 27. Gd and Ho are dispersed evenly throughout each sphere. After 1000 hr the Gd and Ho were still dispersed evenly throughout each individual sphere. The primary 5 Gd sphere at 1000 hrs had a comparatively low amount of Gd, but a secondary sphere imaged showed the same consistent levels throughout the entirety of the body. The primary conclusion drawn from these maps is that the spherization process does not have a large effect on the randomness of the glass network. As controlled consistency throughout the sphere is key for medical applications this is a promising result for the viability of the spheres in hyperthermal treatment.

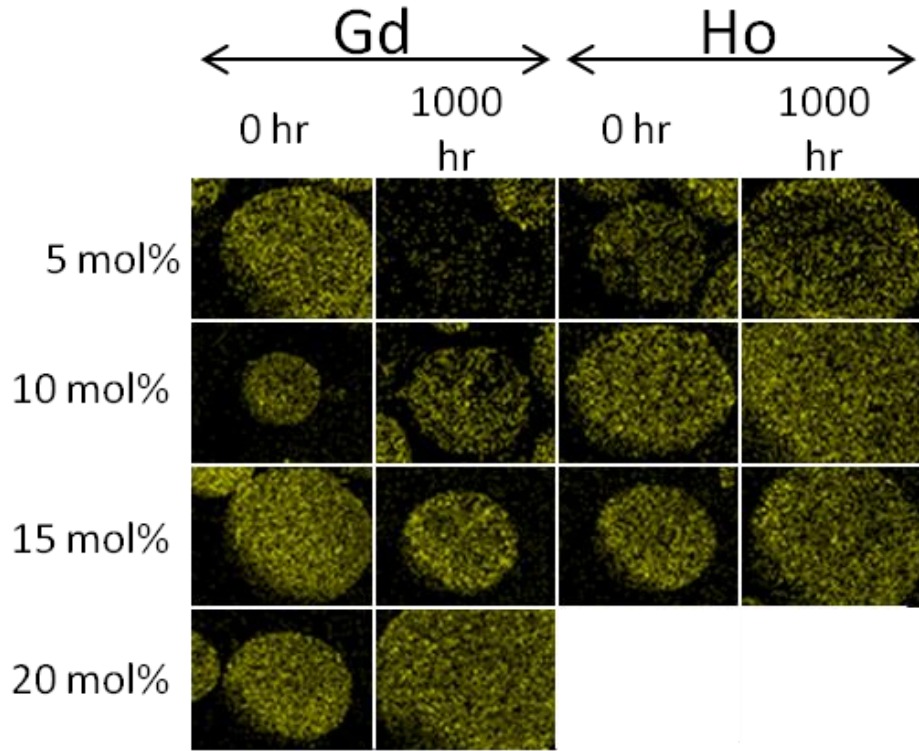


Figure 27. Elemental maps of random Gd and Ho microspheres before and after 1000 hours in DI water.

The SEM analysis was done in complementary to the optical microscopy imaging. Backscattered electron imaging showed remarkable consistency of the composition throughout each microsphere. While the majority of the spheres created were in fact

spheres there were also many different defects. A broad view of the spheres can be seen in Figure 28. There is a high proportion of successfully created spheres to that of those that did not form. The square on the SEM image signifies spheres that did not melt during the spherization process. They have sharp edges and look like regular ground glass powdered particles. Triangles indicates a deviation from perfect sphere that is not a pure non-melting issue. This indicates that an in-congruency in heating occurs where one side melts and the other stays in its powdered form. Others can be seen as ovular demonstrating that a melting process did occur. With these it is likely that the whole particle achieved its melting temperature but did not have time for the surface tension to form a perfect sphere. The most common deviation from perfect sphere is small surface pores. These defects are denoted by the star in Figure 28. These pores are not an issue for the application of cancer hyperthermia. While the previously mentioned defects reduce the consistency of the sizing these pores do not affect the overall size. In any field, and especially the medical field, being able to provide consistently sized samples will yield better results. A potential issue with the pores is that it locally increases the surface area of the sample which could increase the degradation rate of the sphere. This was not noticed to be the case in the corrosion studies, but it could become an issue when translating it to longer time spans. The fourth common defect noticed was a combination of large pores and air-bubbles, and these are denoted by a diamond in Figure 28. Some of these air bubbles extend out onto the surface which causing pores. EDX analysis of these had a larger oxygen concentration than that of the bulk sample, suggesting that the oxygen gas of the flame was incorporated into the sphere.

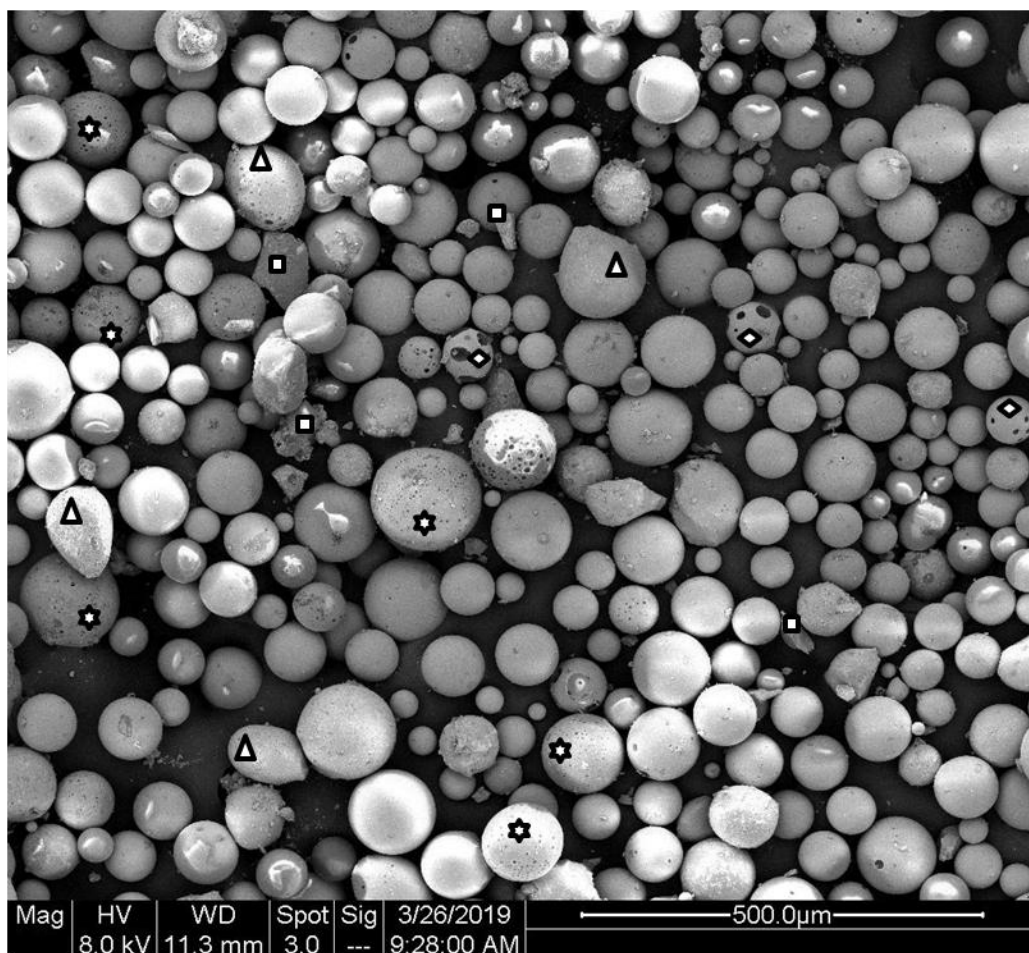


Figure 28. Combination BSE and SE of a broad section of microspheres with typical defects listed. Square: un-melted, triangle: shape, star: pores, diamond: air bubbles.

The aforementioned defects of the spheres were the most common types, but there were also some seldom found defects observed. The first is an offshoot of the typical pores and air bubbles defects. A scaffold structure can be seen in Figure 29 where the pores overtake the entire structure of the microsphere. The left example was from a 15 Ho sample where the overall sphere shape is still seen, but at least a third of the sphere is missing. The sphere on the right was from a 15 Gd after 10hr in a pH 10 solution. It is highly unlikely that the solution caused these changes, the defect is just extremely rare and happened to be put into the solution. It is unclear what the mechanism behind forming this scaffold like structure is, but these samples definitely pose a risk to using the microspheres for cancer hyperthermia. The surface area is increased even more than the

pore defect and corrosion can simultaneously occur internally and externally on the sphere.

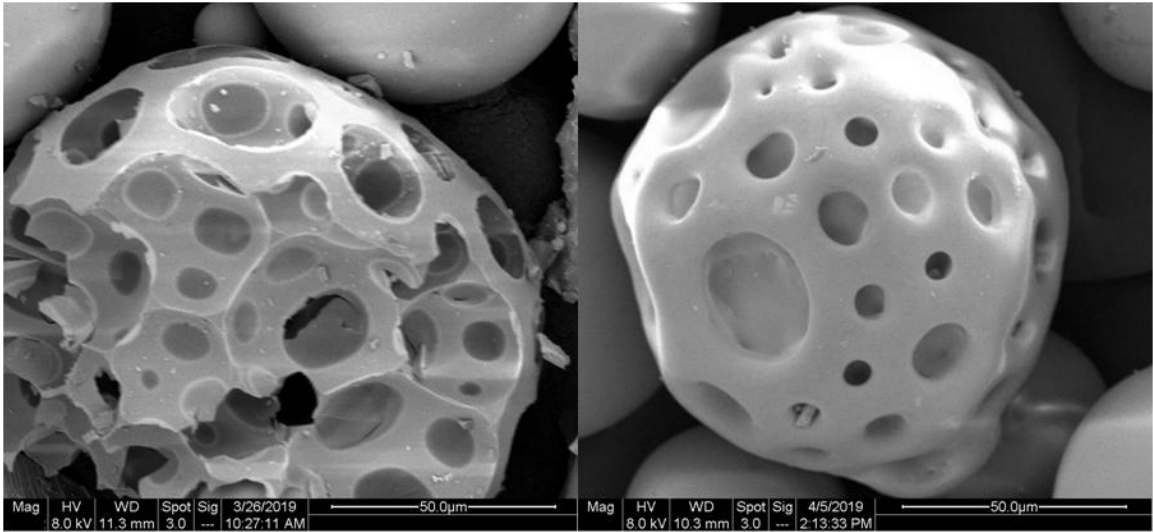


Figure 29. Combination BSE and SE image of a scaffold defect found in 15 Ho (left) and 15 Gd (right) microspheres.

The other rare defect type is related to the air bubble defect. Usually the air bubble defect will have a few smaller bubbles internally but sometimes, as seen in Figure 30, a single large pocket will form that breaches the external of the sphere. These so-called pocket defects can easily be filled. While the 20 Mn sample on the left was filled with a sphere, the defect on 15 Gd sample on the right has a sphere as well as some non-spherized glass frit in it. The pocket defect brings about the same potential issue of increasing the surface area as the scaffold defect, but it also has another associated risk. Being able to attach other particles into the pocket dramatically lowers the control over these set of spheres. It will greatly increase the difficulty in cleaning resulting in an increase of foreign particles entering into the process. A case was found, similar to the pocket defect, where one part of the sphere turned convex. This 15 Ho sample can be seen in Figure 31. These special defect cases were all found in samples with greater than or equal to 15 mol% of the substituent ion, but their rarity does not allow for conclusions to be reliably drawn.

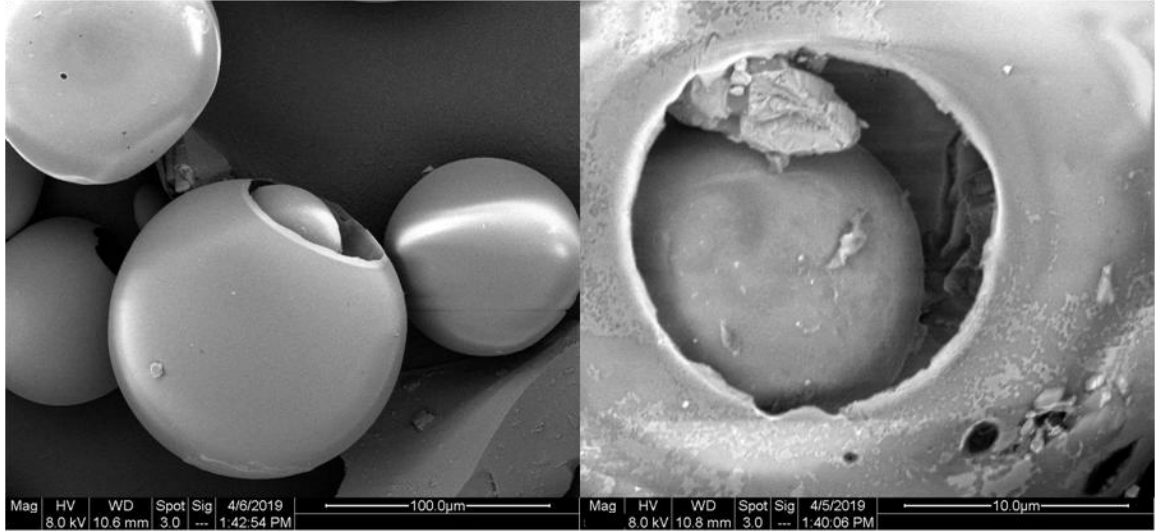


Figure 30 Combination BSE and SE image of pocket defect found in 20 Mn (left) and 15 Gd (right).

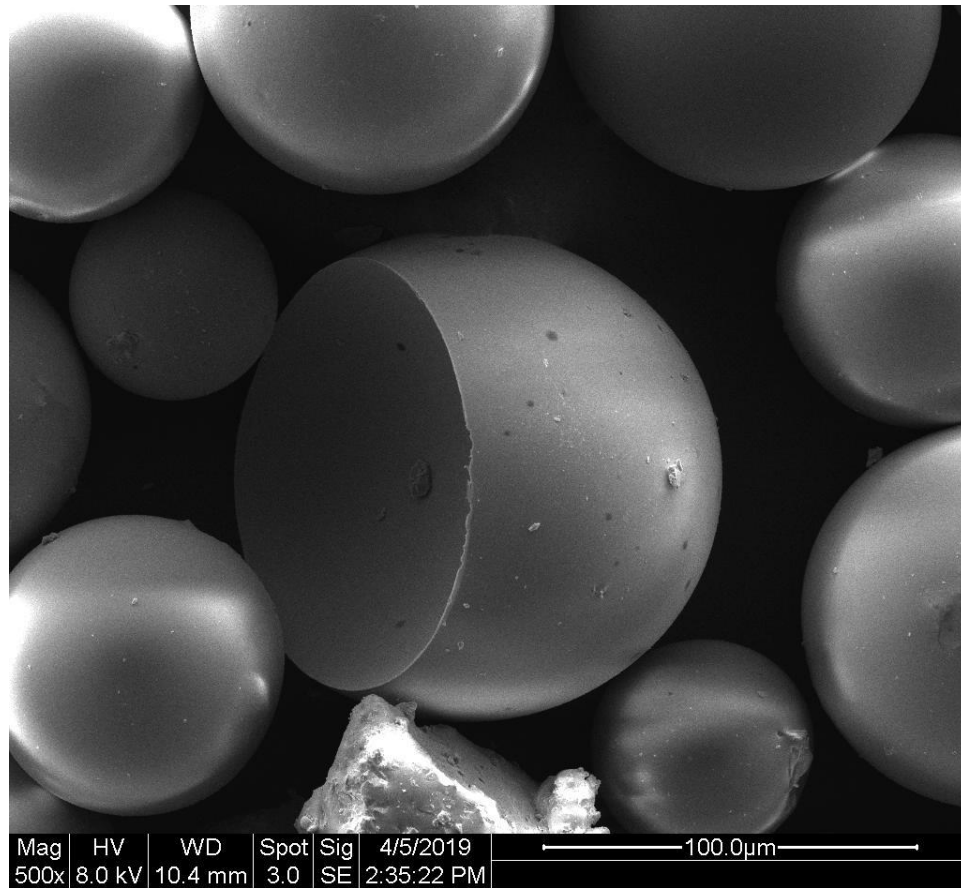


Figure 31. SEM imaging with secondary electrons of a concave sphere defect.

IV. SUMMARY AND CONCLUSIONS

Sixteen compositions of glass were synthesized using the melt-quench method. The compositions were 30SiO₂-10P₂O₅-25GeO₂-35CaO (mol%) with an increasing 5% substituent (Gd₂O₃, Ho₂O₃, Fe₂O₃, and Mn₂O₃) in place of CaO. X-ray diffraction was conducted on the glasses to characterize the structural arrangement within the glass-ceramics. The samples were semi-crystalline with calcium phosphate being the predominant crystalline phase. Thermal analysis was conducted on the glasses and the glass transition temperatures ranged from 590 to 890 °C. There was a decreasing trend for T_g as the concentration of the substituent ion increased. Ion release studies were conducted with inductively coupled plasma optical emission spectroscopy on the glass powder when normalized to the surface area. These studies were for 1, 10, 100, and 1000 hr with water as the suspension medium. The amount of Si, Ge, and substituent ions were determined, and there was a decreasing trend of ion release with increasing Gd and Ho concentration. X-ray photoelectron spectroscopy was conducted on the glass samples and the content of non-bridging oxygen was found by observing the O s1 peak. There was a slight decrease in NBO content with increasing Gd, but the complex network disallowed for conclusions to be reliably drawn.

The sixteen glass compositions were then fabricated into microspheres using the flame spherization method. Optical transmission microscopy showed that the glass was successfully converted into spheres. The size of the spheres was independent of the T_g or the composition and the overall average of the 16 compositions was 95.6 μm. A corrosion study was conducted for 1, 10, 100, and 1000 hr and the samples were analyzed with a scanning electron microscope. There was only slight evidence of corrosion in the samples at pH 4 but it was rarely found. SEM analysis also provided insights into the main types of defects found in the spherization process. The typical defects were total failure to melt, partial melting, surface pores, and air bubbles. There were also atypical scaffold, pocket, and concave defects. Backscattered electrons showed excellent compositional consistency across the individual microspheres. Energy dispersive x-ray spectroscopy was conducted on the samples and the expected increasing substituent content was found across all samples which signified the substituent was not lost during

the spherization process. Based on the characterization of the samples the 10,15,20 Gd and 10,15 Ho samples have the highest potential for success as safe candidates for hyperthermal cancer treatment.

V. FUTURE WORK

The primary future work is a direct continuation of these compositions. Cell viability testing is an important test, as these spheres are intended to stay in the body. Ensuring the glass only kill cells when under a magnetic field is useful not only in its application, but important to know to help calibrate its heating, killing effect on the cells. The spheres will also need to be tested in an MRI to test the effectiveness of the heating of the spheres. MRI testing is important as this is the equipment that would be used for this treatment in hospitals around the globe. This directly related set of work will also give rise to other side projects. The most effective composition in heating will need to be produced on a larger scale. While producing more spheres takes additional time, it also gives much more freedom in the post processing of the spheres. A cleaning and sorting system can be developed to allow for the analysis of specific sizes of spheres. Conducting the experiments with highly controlled sizes may have an effect on any or all of the properties of the spheres.

Other work that can complement this work on glass microspheres for cancer hyperthermia, is a deeper study on the production of microspheres. Already side research has shown changing particle size can increase the yield from 67 to 90%. Using a simpler silicate glass series with changing T_g may also increase the overall and percent spherical yield. A glass series like this may also be able to determine the relation of the composition to any of the defects. Removing the pores and bubbles would be a useful way to increase the viability of these spheres. It could potentially lower the corrosion rate, which was explored earlier, or it could help spheres be used in applications of low refractive indices. Determining what causes these defects could also be useful for drug delivery or bone scaffold applications. The scaffold defect, while rare in this work, could be a very useful device as its shape allows for other materials to be loaded into it. Being able to reliably replicate this defect, and turning it into the product would greatly increase the fundamental understanding of microspheres. There are other potential processing changes that could be made and studying their effects on morphology, yield, size, composition, etc. Some of these processing changes include: preheating the spheres

before they reach the flame, directly quenching the spheres after they exit the flame, doping the spheres while the base glass is on the feed, or changing the amount of time the glass stays in the flame just to name a few. There is a lot of potential in being able to control microsphere processing so any work in this regard can be very valuable to the field.

VI. REFERENCES

1. J. M. Anderson, "Biological Responses to Materials. ," *Annu. Rev. Mater. Res*, **31** [81] 110 (2001).
2. S. Hwang, S. H. Lim, and S. Han, "Highly Adhesive and Bioactive Ti–Mg Alloy Thin Film on Polyether Ether Ketone Formed by PIII&D Technique," *Appl. Surf. Sci.*, **471**, 878-86 (2019).
3. L. L. Hench, "Genetic Design of Bioactive Glass," *J. Eur. Ceram. Soc.*, **29** [7] 1257-65 (2009).
4. "Glass Scaffolds Help Heal Bone," *Am. Ceram. Soc. Bull.*, **92** [8] 16- (2013).
5. T. Keenan, "Dextran-Based Hydrogels for in-Situ Delivery of Gallium-Containing Bioactive Glasses"; Ph.D. Thesis. Alfred University, Alfred NY, 2016.
6. L. L. Hench, N. Roki, and M. B. Fenn, "Bioactive Glasses: Importance of Structure and Properties in Bone Regeneration," *J. Mol. Struct.*, **1073**, 24-30 (2014).
7. J. Park and J. Bronzino, *Biomaterials: Principles and Applications*, Vol. 1; pp. 29. CNC Press, Washington D.C., 2003.
8. R. Lewandowski, J. Minocha, K. Memon, A. Riaz, V. Gates, R. Ryu, K. Sato, R. Omary, and R. Salem, "Sustained Safety and Efficacy of Extended-Shelf-Life Y Glass Microspheres: Long-Term Follow-up in a 134-Patient Cohort," *Eur. J. Nucl. Med. Mol. Imaging*, **41** [3] 486-93 (2014).
9. A. Kennedy, S. Nag, R. Salem, R. Murthy, A. J. McEwan, C. Nutting, A. Benson, J. Espat, J. I. Bilbao, R. A. Sharma, J. P. Thomas, and D. Coldwell, "Recommendations for Radioembolization of Hepatic Malignancies Using Yttrium-90 Microsphere Brachytherapy: A Consensus Panel Report from the Radioembolization Brachytherapy Oncology Consortium," *Int. J. Radiat. Oncol., Biol., Phys.*, **68** [1] 13-23 (2007).
10. R. Damm, R. Seidensticker, G. Ulrich, L. Breier, I. G. Steffen, M. Seidensticker, B. Garlipp, K. Mohnike, M. Pech, H. Amthauer, and J. Ricke, "Y90 Radioembolization in Chemo-Refractory Metastatic, Liver Dominant Colorectal Cancer Patients: Outcome Assessment Applying a Predictive Scoring System," *BMC Cancer*, **16**, 1-7 (2016).
11. D. MacMahon, "Half-Life Evaluations for 3h, 90Sr, and 90Y," *Appl. Radiat. Isot.*, **64** [10] 1417-9 (2006).

12. L. Sanche, "Interaction of Low Energy Electrons with DNA: Applications to Cancer Radiation Therapy," *Radiat. Phys. Chem.*, **128**, 36-43 (2016).
13. B. Hildebrandt, P. Wust, O. Ahlers, A. Dieing, G. Sreenivasa, T. Kerner, R. Felix, and H. Riess, "The Cellular and Molecular Basis of Hyperthermia," *Crit. Rev. Oncol. Hematol.*, **43** [1] 33-56 (2002).
14. P. Das, M. Colombo, and D. Prosperi, "Recent Advances in Magnetic Fluid Hyperthermia for Cancer Therapy," *Colloids Surf., B*, **174**, 42-55 (2019).
15. C. Fernandez and N. J. Beeching, "Pyrexia of Unknown Origin," *Clin. Med.*, **18** [2] 170-4 (2018).
16. D. Zhao, W. Huang, M. N. Rahaman, D. E. Day, D. Wang, and Y. Gu, "Preparation and Characterization of Composite Microspheres for Brachytherapy and Hyperthermia Treatment of Cancer," *Mater. Sci. Eng. C.*, **32** [2] 276-81 (2012).
17. D. Arce, P. Cacchiarelli, G. Pratta, F. Spetale, F. Krsticevic, E. Tapia, J. D. Las Rivas, and S. Ponce, "Regulatory Motifs Found in the Small Heat Shock Protein (sHSP) Gene Family in Tomato," *BMC Genomics*, **19** [1] 1-7 (2018).
18. A. Ito, F. Matsuoka, H. Honda, and T. Kobayashi, "Heat Shock Protein 70 Gene Therapy Combined with Hyperthermia Using Magnetic Nanoparticles," *Cancer Gene Ther.*, **10** [12] 918-25 (2003).
19. C. W. Song, "Effect of Local Hyperthermia on Blood Flow and Microenvironment: A Review," *Cancer Res.*, **44** [10 Supplement] 4721s (1984).
20. P. Vaupel, F. Kallinowski, and P. Okunieff, "Blood Flow, Oxygen and Nutrient Supply, and Metabolic Microenvironment of Human Tumors: A Review," *Cancer Res.*, **49** [23] 6449 (1989).
21. N. R. Datta, A. K. Bose, H. K. Kapoor, and S. Gupta, "Head and Neck Cancers: Results of Thermoradiotherapy Versus Radiotherapy," *Int. J. Hyperthermia*, **6** [3] 479-86 (1990).
22. D. S. Kapp, I. A. Petersen, R. S. Cox, G. M. Hahn, P. Fessenden, S. D. Prionas, E. R. Lee, J. L. Meyer, T. V. Samulski, and M. A. Bagshaw, "Two or Six Hyperthermia Treatments as an Adjunct to Radiation Therapy Yield Similar Tumor Responses: Results of a Randomized Trial," *Int. J. Radiat. Oncol., Biol., Phys.*, **19** [6] 1481-95 (1990).
23. B. A. Berdov and G. Z. Menteshashvili, "Thermoradiotherapy of Patients with Locally Advanced Carcinoma of the Rectum," *Int. J. Hyperthermia*, **6** [5] 881-90 (1990).

24. R. Valdagni and M. Amichetti, "Report of Long-Term Follow-up in a Randomized Trial Comparing Radiation Therapy and Radiation Therapy Plus Hyperthermia to Metastatic Lymphnodes in Stage IV Head and Neck Patients," *Int. J. Radiat. Oncol., Biol., Phys.*, **28** [1] 163-9 (1994).
25. J. Overgaard, S. M. Bentzen, J. Overgaard, D. Gonzalez Gonzalez, M. C. C. M. Hulshof, G. Arcangeli, O. Dahl, and O. Mella, "Randomised Trial of Hyperthermia as Adjuvant to Radiotherapy for Recurrent or Metastatic Malignant Melanoma," *The Lancet*, **345** [8949] 540-3 (1995).
26. C. C. Vernon, J. W. Hand, S. B. Field, D. Machin, J. B. Whaley, J. van der Zee, W. L. J. van Putten, G. C. van Rhoon, J. D. P. van Dijk, D. G. González, F.-F. Liu, P. Goodman, and M. Sherar, "Radiotherapy with or without Hyperthermia in the Treatment of Superficial Localized Breast Cancer: Results from Five Randomized Controlled Trials," *Int. J. Radiat. Oncol., Biol., Phys.*, **35** [4] 731-44 (1996).
27. P. K. Sneed, P. R. Stauffer, M. W. McDermott, C. J. Diederich, K. R. Lamborn, M. D. Prados, S. Chang, K. A. Weaver, L. Spry, M. K. Malec, S. A. Lamb, B. Voss, R. L. Davis, W. M. Wara, D. A. Larson, T. L. Phillips, and P. H. Gutin, "Survival Benefit of Hyperthermia in a Prospective Randomized Trial of Brachytherapy Boost \pm Hyperthermia for Glioblastoma Multiforme," *Int. J. Radiat. Oncol., Biol., Phys.*, **40** [2] 287-95 (1998).
28. J. van der Zee, D. González, G. C. van Rhoon, J. D. P. van Dijk, W. L. J. van Putten, and A. A. M. Hart, "Comparison of Radiotherapy Alone with Radiotherapy Plus Hyperthermia in Locally Advanced Pelvic Tumours: A Prospective, Randomised, Multicentre Trial," *The Lancet*, **355** [9210] 1119-25 (2000).
29. E. L. Jones, J. R. Oleson, L. R. Prosnitz, T. V. Samulski, Z. Vujaskovic, D. Yu, L. L. Sanders, and M. W. Dewhirst, "Randomized Trial of Hyperthermia and Radiation for Superficial Tumors," *J. Clin. Oncol.*, **23** [13] 3079-85 (2005).
30. A. Attaluri, S. K. Kandala, M. Wabler, H. Zhou, C. Cornejo, M. Armour, M. Hedayati, Y. Zhang, T. L. DeWeese, C. Herman, and R. Ivkov, "Magnetic Nanoparticle Hyperthermia Enhances Radiation Therapy: A Study in Mouse Models of Human Prostate Cancer," *Int. J. Hyperthermia*, **31** [4] 359-74 (2015).
31. K. Mahmoudi, A. Bouras, D. Bozec, R. Ivkov, and C. Hadjipanayis, "Magnetic Hyperthermia Therapy for the Treatment of Glioblastoma: A Review of the Therapy's History, Efficacy and Application in Humans," *Int. J. Hyperthermia*, **34** [8] 1316-28 (2018).

32. S. Jha, P. K. Sharma, and R. Malviya, "Hyperthermia: Role and Risk Factor for Cancer Treatment," *Achiev. Life Sci.*, **10** [2] 161-7 (2016).
33. U. O. Häfeli, M. A. Lobedann, J. Steingroewer, L. R. Moore, and J. Riffle, "Optical Method for Measurement of Magnetophoretic Mobility of Individual Magnetic Microspheres in Defined Magnetic Field," *J. Magn. Magn. Mater.*, **293** [1] 224-39 (2005).
34. D. Zahn, A. Weidner, Z. Nosrati, L. Wöckel, J. Dellith, R. Müller, K. Saatchi, U. O. Häfeli, and S. Dutz, "Temperature Controlled Camptothecin Release from Biodegradable Magnetic PLGA Microspheres," *J. Magn. Magn. Mater.*, **469**, 698-703 (2019).
35. Z. Shaterabadi, G. Nabiyouni, and M. Soleymani, "Physics Responsible for Heating Efficiency and Self-Controlled Temperature Rise of Magnetic Nanoparticles in Magnetic Hyperthermia Therapy," *Prog. Biophys. Mol. Biol.*, **133**, 9-19 (2018).
36. A. Goldman, *Modern Ferrite Technology*, 2nd ed.; pp. 309-10. Springer Science & Business Media, Pittsburgh PA, 2006.
37. S. Laurent, S. Dutz, U. O. Häfeli, and M. Mahmoudi, "Magnetic Fluid Hyperthermia: Focus on Superparamagnetic Iron Oxide Nanoparticles," *Adv. Colloid Interface Sci.*, **166** [1] 8-23 (2011).
38. A. Hervault and N. T. K. Thanh, "Magnetic Nanoparticle-Based Therapeutic Agents for Thermo-Chemotherapy Treatment of Cancer," *Nanoscale*, **6** [20] 11553-73 (2014).
39. E. Y. Chang and B. A. Jobe, "Esophageal Imaging: Functional--MRI"; pp. 179-83 in *Esophageal Cancer: Principles & Practice*. Demos Medical Publishing, LLC., New York, NY, 20, 2009.
40. A. Guarise and G. Morana, "Magnetic Resonance Imaging"; pp. 109-29 in *Biliary Tract and Gallbladder Cancer: Diagnosis and Therapy*. Edited by C. R. Thomas. Demos Medical Publishing, LLC., New York, NY, 2009.
41. D. M. Minca, E. L. Enache, F. Tatu, and C. Tatu, "Gadolinium-Based Contrast Agents: Safety, Efficacy and Potential Adverse Events," *Fiziologia.*, **24** [2] 31-7 (2014).
42. J. Wang, B. Xiang, H.-Y. Lin, H. Liu, D. Freed, R. C. Arora, and G. Tian, "Pathological Mechanism for Delayed Hyperenhancement of Chronic Scarred Myocardium in Contrast Agent Enhanced Magnetic Resonance Imaging," *PLoS ONE*, **9** [5] 1-9 (2014).

43. R. Forghani, "Adverse Effects of Gadolinium-Based Contrast Agents: Changes in Practice Patterns," *Top. Magn. Reson. Imaging*, **25** [4] 163-9 (2016).
44. B. Zhang, L. Liang, W. Chen, C. Liang, and S. Zhang, "An Updated Study to Determine Association between Gadolinium-Based Contrast Agents and Nephrogenic Systemic Fibrosis," *PLoS ONE*, **10** [6] 1-15 (2015).
45. L. M. B. Burke, M. Ramalho, M. AlObaidy, E. Chang, M. Jay, and R. C. Semelka, "Self-Reported Gadolinium Toxicity: A Survey of Patients with Chronic Symptoms," *Magn. Reson. Imaging*, **34** [8] 1078-80 (2016).
46. T. Kanda, T. Fukusato, M. Matsuda, K. Toyoda, H. Oba, and J. Kotoku, "Gadolinium-Based Contrast Agent Accumulates in the Brain Even in Subjects without Severe Renal Dysfunction: Evaluation of Autopsy Brain Specimens with Inductively Coupled Plasma Mass Spectroscopy," *Radiology*, **276** [1] 228-32 (2015).
47. T. Kanda, Y. Nakai, H. Oba, K. Toyoda, K. Kitajima, and S. Furui, "Gadolinium Deposition in the Brain," *Magn. Reson. Imaging*, **34** [10] 1346-50 (2016).
48. J. Kurtkoti, T. Snow, and B. Hiremagalur, "Gadolinium and Nephrogenic Systemic Fibrosis: Association or Causation (Review Article)," *Nephrology*, **13** [3] 235-41 (2008).
49. "FDA Drug Safety Communication: New Warnings for Using Gadolinium-Based Contrast Agents in Patients with Kidney Dysfunction" (2010) Accessed on: Apr. 2019. Available at <<https://www.fda.gov/Drugs/DrugSafety/ucm223966.htm>>
50. A. Timur Sh, Y. C. Shin, S. Su-Jin, H. Dong-Wook, and H. H. Nguyen, "Toxicity and T2-Weighted Magnetic Resonance Imaging Potentials of Holmium Oxide Nanoparticles," *Nanomaterials*, **7** [8] 216 (2017).
51. A. J. A. T. Braat, J. F. Prince, R. van Rooij, R. C. G. Bruijnen, M. A. A. J. van den Bosch, and M. G. E. H. Lam, "Safety Analysis of Holmium-166 Microsphere Scout Dose Imaging During Radioembolisation Work-Up: A Cohort Study," *Eur. Radiol.*, **28** [3] 920-8 (2018).
52. T. Miyamachi, T. Schuh, T. Märkl, C. Bresch, T. Balashov, A. Stöhr, C. Karlewski, S. André, M. Marthaler, M. Hoffmann, M. Geilhufe, S. Ostanin, W. Hergert, I. Mertig, G. Schön, A. Ernst, and W. Wulfhekel, "Stabilizing the Magnetic Moment of Single Holmium Atoms by Symmetry," *Nature*, **503** [7475] 242-6 (2013).

53. M. Alhamami, W. Cheng, Y. Lyu, C. Allen, X. Zhang, and H.-L. M. Cheng, "Manganese-Porphyrin-Enhanced MRI for the Detection of Cancer Cells: A Quantitative in Vitro Investigation with Multiple Clinical Subtypes of Breast Cancer," *PLoS ONE*, **13** [5] 1-17 (2018).
54. S. C. Iriah, M. Trivedi, W. Kenkel, S. E. Grant, K. Moore, J. R. Yee, D. Madularu, P. Kulkarni, and C. F. Ferris, "Oxycodone Exposure: A Magnetic Resonance Imaging Study in Response to Acute and Chronic Oxycodone Treatment in Rats," *Neuroscience*, **398**, 88-101 (2019).
55. L. Morrow, B. Snow, A. Ali, S. J. Maguire-Boyle, Z. Almutairi, D. K. Potter, and A. R. Barron, "Temperature Dependence on the Mass Susceptibility and Mass Magnetization of Superparamagnetic Mn-Zn-Ferrite Nanoparticles as Contrast Agents for Magnetic Imaging of Oil and Gas Reservoirs," *J. Exp. Nanosci.*, **13** [1] 107-18 (2018).
56. S. Kikuta, Y. Yanagawa, N. Homma, and M. Osanai, "Evaluation of the Amount of the Manganese Entry in the Neurons for Activity-Induced Manganese-Enhanced MRI," *Electron. Commun. Jpn.*, **99** [8] 48-53 (2016).
57. M. Sane, K. Malukani, R. Kulkarni, and A. Varun, "Fatal Iron Toxicity in an Adult: Clinical Profile and Review," *Indian J. Crit. Care Med.*, **22** [11] 801-3 (2018).
58. B. Getachew, A. B. Csoka, M. Aschner, and Y. Tizabi, "Nicotine Protects Against Manganese and Iron-Induced Toxicity in SH-SY5Y Cells: Implication for Parkinson's Disease," *Neurochem. Int.*, **124**, 19-24 (2019).
59. A. T. Mohammed, L. L. M. Ebraheim, and M. M. M. Metwally, "Ebselen Can Protect Male Reproductive Organs and Male Fertility from Manganese Toxicity: Structural and Bioanalytical Approach in a Rat Model," *Biomed. Pharmacother.*, **102**, 739-48 (2018).
60. A. W. Wren, M. C. Jones, S. T. Mixture, A. Coughlan, N. L. Keenan, M. R. Towler, and M. M. Hall, "A Preliminary Investigation into the Structure, Solubility and Biocompatibility of Solgel SiO₂-CaO-Ga₂O₃ Glass-Ceramics," *Mater. Chem. Phys.*, **148** [1] 416-25 (2014).
61. S. S. Chon, L. Piraino, S. Mokhtari, E. A. Krull, A. Coughlan, Y. Gong, N. P. Mellott, T. J. Keenan, and A. W. Wren, "Synthesis, Characterization and Solubility Analysis of Amorphous SiO₂-CaO-Na₂O-P₂O₅ Scaffolds for Hard Tissue Repair," *J. Non-Cryst. Solids*, **490**, 1-12 (2018).

62. Y. Li, A. Coughlan, F. R. Laffir, D. Pradhan, N. P. Mellott, and A. W. Wren, "Investigating the Mechanical Durability of Bioactive Glasses as a Function of Structure, Solubility and Incubation Time," *J. Non-Cryst. Solids*, **380**, 25-34 (2013).
63. M. Szumera, I. Waclawska, and J. Sułowska, "Thermal Properties of MnO and SiO Containing Phosphate Glasses," *J. Therm. Anal. Calorim.*, **123** [2] 1083-9 (2016).
64. Y. F. Ma, P. Yu, and L. Xia, "Achieving the Best Glass Former in a Binary Gd–Co Alloy System," *Mater. Des.*, **85**, 715-8 (2015).
65. K. Nitsch, A. Cihlář, D. Klimm, M. Nikl, and M. Rodová, "Na-Gd Phosphate Glasses," *J. Therm. Anal. Calorim.*, **80** [3] 735-8 (2005).
66. Y. Zhang and A. Navrotsky, "Thermochemistry of Rare-Earth Aluminate and Aluminosilicate Glasses," *J. Non-Cryst. Solids*, **341** [1] 141-51 (2004).
67. E. Malchukova and B. Boizot, "B-Irradiation Effect in Aluminoborosilicate Glasses: The Role of Re Codoping (Re = Sm, Gd)," *Phys. Solid State*, **50** [9] 1687-91 (2008).
68. S. Rada, T. Ristoiu, M. Rada, I. Coroiu, V. Maties, and E. Culea, "Towards Modeling Gadolinium–Lead–Borate Glasses," *Mater. Res. Bull.*, **45** [1] 69-73 (2010).
69. Y. Lai, X. Liang, S. Yang, P. Liu, Y. Zeng, and C. Hu, "Raman and FTIR Spectra of CeO₂ and Gd₂O₃ in Iron Phosphate Glasses," *J. Alloys Compd.*, **617**, 597-601 (2014).
70. H. Zhang, R. Li, Y. Ji, F. Liu, Q. Luo, and T. Zhang, "Glass Formation, Magnetic Properties and Magnetocaloric Effect of Ternary Ho–Al–Co Bulk Metallic Glass," *J. Magn. Magn. Mater.*, **324** [23] 4064-7 (2012).
71. A. A. Alemi, H. Sedghi, A. R. Mirmohseni, and V. Golsanamlu, "Synthesis and Characterization of Holmium Oxide Doped Cadmium Lead Borate Glasses," *Radiat. Eff. Defects Solids*, **162** [5] 351-8 (2007).
72. M. T. Nayak, J. A. E. Desa, V. R. Reddy, C. Nayak, D. Bhattacharyya, and S. N. Jha, "Structures of Silicate Glasses with Varying Sodium and Fixed Iron Contents," *J. Non-Cryst. Solids*, **509**, 42-7 (2019).
73. J. A. Johnson, C. E. Johnson, D. Holland, A. Mekki, P. Appleyard, and M. F. Thomas, "Transition Metal Ions in Ternary Sodium Silicate Glasses: A Mössbauer and Neutron Study," *J. Non-Cryst. Solids*, **246** [1] 104-14 (1999).

74. P. A. Bingham, J. M. Parker, T. Searle, J. M. Williams, and K. Fyles, "Redox and Clustering of Iron in Silicate Glasses," *J. Non-Cryst. Solids*, **253** [1] 203-9 (1999).
75. B. Barrioni, A. Oliveira, M. Fátima Leite, and M. Magalhães Pereira, "Sol-Gel-Derived Manganese-Releasing Bioactive Glass as a Therapeutic Approach for Bone Tissue Engineering," *J. Mater. Sci.*, **52** [15] 8904-27 (2017).
76. I. Zaitizila, M. K. Halimah, F. D. Muhammad, and M. S. Nurisya, "Influence of Manganese Doping on Elastic and Structural Properties of Silica Borotellurite Glass," *J. Non-Cryst. Solids*, **492**, 50-5 (2018).
77. J. E. Shelby, *Introduction to Glass Science and Technology*, 2nd ed.; pp. 9-11. The Royal Society of Chemistry, Cambridge UK, 2005.
78. H. W. Nesbitt, G. M. Bancroft, G. S. Henderson, R. Ho, K. N. Dalby, Y. Huang, and Z. Yan, "Bridging, Non-Bridging and Free (O²⁻) Oxygen in Na₂O-SiO₂ Glasses: An X-Ray Photoelectron Spectroscopic (XPS) and Nuclear Magnetic Resonance (NMR) Study," *J. Non-Cryst. Solids*, **357** [1] 170-80 (2011).
79. R. Sawyer, H. W. Nesbitt, and R. A. Secco, "High Resolution X-Ray Photoelectron Spectroscopy (XPS) Study of K₂O-SiO₂ Glasses: Evidence for Three Types of O and at Least Two Types of Si," *J. Non-Cryst. Solids*, **358** [2] 290-302 (2012).
80. A. Das, P. S. R. Krishna, M. Goswami, and M. Krishnan, "Structural Analysis of Al and Si Substituted Lithium Germanium Phosphate Glass-Ceramics Using Neutron and X-Ray Diffraction," *J. Solid State Chem.*, **271**, 74-80 (2019).
81. J. Alvarado-Rivera, D. A. Rodríguez-Carvajal, M. d. C. Acosta-Enríquez, M. B. Manzanares-Martínez, E. Álvarez, R. Lozada-Morales, G. C. Díaz, A. Leon, M. E. Zayas, and J. Mauro, "Effect of CeO₂ on the Glass Structure of Sodium Germanate Glasses," *J. Am. Ceram. Soc.*, **97** [11] 3494-500 (2014).
82. H. M. Wang and G. S. Henderson, "Investigation of Coordination Number in Silicate and Germanate Glasses Using O K-Edge X-Ray Absorption Spectroscopy," *Chem. Geol.*, **213** [1] 17-30 (2004).
83. J. G. Penfield and R. F. Reilly Jr, "What Nephrologists Need to Know About Gadolinium," *Nat. Clin. Pract. Nephrol.*, **3** [12] 654-68 (2007).
84. L. M. Haas, C. M. Smith, L. M. Placek, M. M. Hall, Y. Gong, N. P. Mellott, and A. W. Wren, "Investigating the Effect of Silver Coating on the Solubility, Antibacterial Properties, and Cytocompatibility of Glass Microspheres," *J. Biomater. Appl.*, **30** [4] 450-62 (2015).

85. H. Zhang, T. Wang, Y. Zheng, C. Yan, W. Gu, and L. Ye, "Comparative Toxicity and Contrast Enhancing Assessments of Gd₂O₃@BSA and MnO₂@BSA Nanoparticles for MR Imaging of Brain Glioma," *Biochem. Biophys. Res. Commun.*, **499** [3] 488-92 (2018).
86. M. Birka, J. Roscher, M. Holtkamp, M. Sperling, and U. Karst, "Investigating the Stability of Gadolinium Based Contrast Agents Towards UV Radiation," *Water Res.*, **91**, 244-50 (2016).
87. S. Kubuki, K. Akagi, H. Sakka, Z. Homonnay, K. Sinkó, E. Kuzmann, H. Kurimoto, and T. Nishida, "Dissolution Behaviour of Iron Silicate Glass," *Hyperfine Interact.*, **192** [1-3] 31-6 (2009).
88. S. K. Morcos and H. S. Thomsen, "Nephrogenic Systemic Fibrosis: More Questions and Some Answers," *Nephron Clin. Pract.*, **110** [1] c24-c32 (2008).